

UniGenX: a unified generative foundation model that couples sequence, structure and function to accelerate scientific design across proteins, molecules and materials

Gongbo Zhang^{1,2,9,*}, Yanting Li^{1,3,*}, Renqian Luo^{1,*,†}, Pipi Hu^{1,10,*,†}, Yang Yang^{1,4,*}, Zeru Zhao⁶, Lingbo Li⁵, Guoqing Liu¹, Zun Wang¹, Ran Bi¹, Kaiyuan Gao⁶, Liya Guo⁷, Yu Xie¹, Chang Liu¹, Jia Zhang¹, Tian Xie¹, Robert Pinsler¹, Claudio Zeni¹, Ziheng Lu¹, Hongxia Hao¹, Yingce Xia¹, Marwin Segler¹, Maik Riechert¹, Wei Yang^{4,6}, Hao Jiang⁸, Wen-Bin Zhang^{8,9}, Zhijun Zeng¹³, Yi Zhu^{7,10}, Li Dong¹¹, Xiuyuan Hu¹², Li Yuan^{2,9}, Lei Chen³, Haiguang Liu¹, Tao Qin¹

¹Microsoft Research AI for Science

²School of Electronic and Computer Engineering, Peking University

³DSA, The Hong Kong University of Science and Technology (Guangzhou)

⁴School of Computer Science and Technology, Huazhong University of Science and Technology

⁵Department of Automation, Tsinghua University

⁶School of Artificial Intelligence and Automation, Huazhong University of Science and Technology

⁷Yau Mathematical Sciences Center, Tsinghua University

⁸Beijing National Laboratory for Molecular Sciences; Key Laboratory of Polymer Chemistry & Physics of Ministry of Education; Center for Soft Matter Science and Engineering; College of Chemistry and Molecular Engineering, Peking University, Beijing

⁹School of AI4S, Shenzhen Graduate School, Peking University, Shenzhen 518055

¹⁰Beijing Institute of Mathematical Sciences and Applications, Beijing 101408

¹¹Microsoft Research Asia

¹²Department of Electronic Engineering, Tsinghua University

¹³Department of Mathematical Sciences, Tsinghua University

*Co-first authors in random order. Work done while Gongbo and Yanting were interns at Microsoft Research AI for Science

†Corresponding authors in random order, Email: renqianluo@gmail.com; hpp@bimsa.cn

Abstract

Function in natural systems arises from one-dimensional sequences forming three-dimensional structures with specific properties. However, current generative models suffer from critical limitations: training objectives seldom target function directly, discrete sequences and continuous coordinates are optimized in isolation, and conformational ensembles are under-modeled. We present UniGenX, a unified generative foundation model that addresses these gaps by co-generating sequences and coordinates under direct functional and property objectives across proteins, molecules, and materials. UniGenX represents heterogeneous inputs as a mixed stream of symbolic and numeric tokens, where a decoder-only autoregressive transformer provides global context and a conditional diffusion head generates numeric fields steered by task-specific tokens. Besides the new high SOTAs on structure prediction tasks, the model demonstrates state-of-the-art or competitive performance for the function-aware generation across domains: in materials,

it achieves “conflicted” multi-property conditional generation, yielding 436 crystal candidates meeting triple constraints, including 11 with novel compositions and 4 confirmed thermodynamically stable by DFT; in chemistry, it sets new benchmarks on five property targets and conformer ensemble generation on GEOM; and in biology, it improves success in modeling protein induced fit ($\text{RMSD} < 2 \text{ \AA}$) by over 23-fold and enhances EC-conditioned enzyme design. Ablation studies and cross-domain transfer substantiate the benefits of joint discrete-continuous training, establishing UniGenX as a significant advance from prediction to controllable, function-aware generation.

Keywords— Unified Generation, Autoregressive Diffusion Model, Next-token Prediction, AI for Science

1 Introduction

The ability of one-dimensional sequences to form three-dimensional structures with specific functions is a fundamental principle in natural systems. Replicating this generative process is a central goal for artificial intelligence in scientific discovery, promising to unlock transformative applications in materials design, drug discovery, and protein engineering [1, 2]. The intricate interplay between a system’s discrete sequence (e.g., chemical formula, amino acid chain) and its continuous coordinates (e.g., atomic positions, protein fold) dictates its essential properties and functions. For instance, a crystal’s atomic arrangement governs its electronic characteristics [3], a molecule’s spatial conformation determines its pharmacological efficacy [4], and a protein’s 3D shape enables its biological role [5]. Given this sensitivity, where even minute deviations in atomic coordinates can nullify function, the challenge is not just to predict structures, but to generate them with high numerical precision under desired functional constraints.

However, current generative models face critical limitations that hinder this goal. First, most training objectives target structural accuracy in isolation, rather than the ultimate function or property of interest. Second, the generation of discrete sequences and continuous coordinates are often treated as separate tasks, failing to capture their co-dependent relationship. Finally, models typically generate a single static structure, under-modeling the dynamic conformational ensembles that are crucial for the function of many molecular and biological systems. These gaps have created a significant bottleneck, preventing a unified approach to controllable, function-aware generation across scientific domains.

The current modeling landscape is dominated by two powerful yet incomplete paradigms. On one hand, autoregressive language models (LLMs) excel at processing and generating discrete token sequences, demonstrating remarkable flexibility, scalability, and long-context reasoning [6, 7]. However, their token-based nature struggles to enforce the strict numerical precision required for generating physically plausible 3D atomic coordinates. On the other hand, diffusion models have achieved state-of-the-art performance in generating high-fidelity continuous data, such as images and 3D structures [8, 9, 10]. Yet, they are less adept at handling discrete sequence information and lack the flexible, token-by-token generative framework of autoregressive models, making the joint generation of sequence and structure challenging.

To address these shortcomings, we introduce UniGenX, a unified generative foundation model that co-generates sequences and coordinates under direct functional and property objectives. UniGenX bridges the gap between discrete and continuous generation by integrating an autoregressive transformer with a conditional diffusion head. In our framework, heterogeneous inputs are represented as a mixed stream of symbolic and numeric tokens. A decoder-only transformer processes this stream to capture global context, while the conditional diffusion head generates precise numeric

fields (i.e., coordinates) steered by task-specific functional tokens. This hybrid architecture synergistically combines the contextual power and flexibility of autoregressive models with the numerical precision of diffusion models, enabling a single framework to operate across proteins, molecules, and materials.

UniGenX marks a significant advance from prediction to controllable, function-aware generation. Beyond setting new state-of-the-art benchmarks on structure prediction tasks, our model demonstrates unparalleled capabilities in conditional generation across domains. In materials science, it successfully navigates “conflicted” multi-property objectives to design 436 novel crystal candidates, including 11 with new compositions and 4 confirmed as thermodynamically stable by DFT calculations. In chemistry, it establishes new performance records on five property-targeting tasks and conformer ensemble generation. For biology, it improves the success rate of modeling protein induced fit ($\text{RMSD} < 2 \text{ \AA}$) by over 23-fold and enhances enzyme design conditioned on Enzyme Commission (EC) numbers. Through extensive ablation studies and cross-domain transfer experiments, we substantiate the benefits of our joint discrete–continuous training strategy, establishing UniGenX as a versatile and powerful foundation for AI-driven scientific discovery.

2 Methods

UniGenX leverages the strengths of both autoregressive (AR) and diffusion models, achieving a natural unification. The diffusion head addresses the numerical precision limitations of general AR models by operating in a continuous vector space for numerical data. Conversely, the AR next-token prediction provides effective conditioning for the diffusion head, which diffuses only a low-dimensional variable (e.g., three dimensions for molecular 3D structures), significantly simplifying the diffusion training process. Our design seamlessly integrates symbolic (words) and numerical (numbers) data across scientific domains without sacrificing scientific precision. This section details the key features of the UniGenX architecture.

2.1 Sequentialize All for Multi-Domain/Task Compatibility

The success of multimodal GPT-like models in integrating language and images demonstrates the potential of sequence alignment for addressing diverse problems across various domains. To achieve alignment with language—a naturally sequential modality—images are encoded into a latent space using a pretrained encoder and subsequently aligned with language embeddings within this shared latent space. This process enables general comprehension and facilitates generation in both language and image modalities. This approach highlights the flexibility of sequentialization across diverse domains and tasks, a principle validated by previous research and applications of GPT models.

However, scientific data presents distinct challenges in sequentialization compared to data from general domains like language, images, and videos. Scientific data exhibits significantly greater complexity and diverse standards across different disciplines. For instance, small molecules are frequently represented using SMILES strings, encoding atoms and chemical bonds [11], while periodic materials are often described by chemical formulas [12], accompanied by atomic coordinates. Proteins, DNA, and data types like energies and forces also utilize specialized, compact representations. This inherent domain specificity and the deep integration of expert knowledge within these representations make establishing a unified standard exceptionally challenging. Consequently, developing a universal representation capable of aligning structures, energies, forces, and other numerical properties with language-like atomic or molecular descriptions is exceedingly difficult. Furthermore, scientific data inherently contains a large amount of numerical data that is highly sensitive to numerical precision.

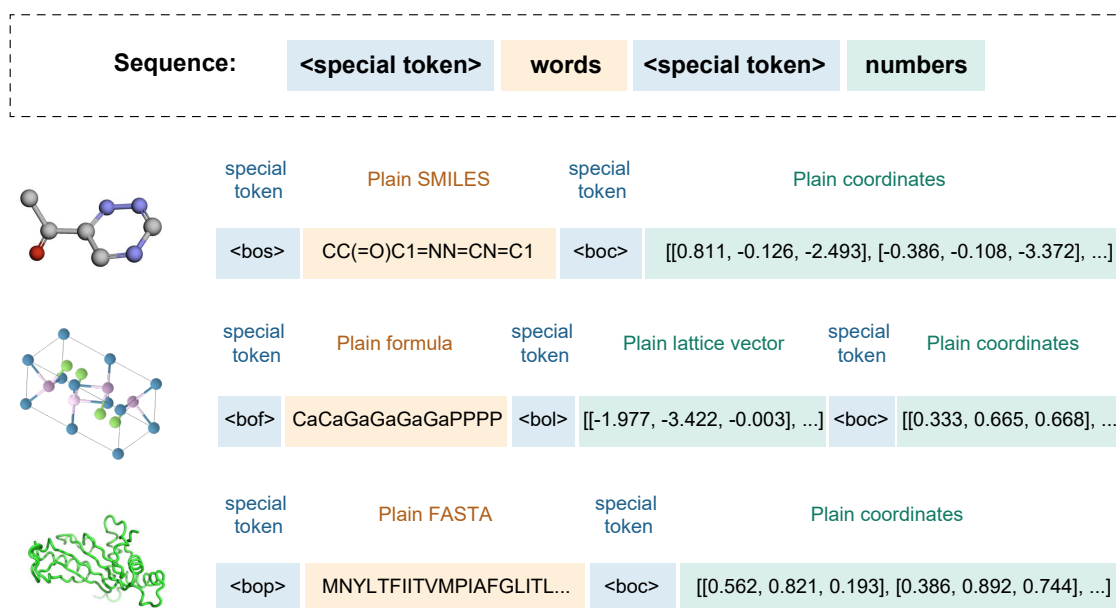


Figure 1: Sequentialization approach combines symbolic (words) and numerical data (numbers), separated by special tokens that identify the category of each data element. As illustrated in the figure for small molecules and materials, SMILES strings or chemical formulas are treated as words and delimited by special tokens such as <bos> (beginning of SMILES) or <bof> (beginning of formula). Corresponding coordinates are treated as numbers, delimited by tokens such as <boc> (beginning of coordinates). This method provides a general framework applicable to diverse scientific data formats.

The aforementioned challenges preclude the direct transfer of sequentialization methods from general domains to scientific applications.

To fully leverage the flexibility of multimodality, we propose a simple yet effective sequentialization approach: representing all data—formulas, coordinates, energies, forces, and so on—as a single sequence segmented by special tokens. This sequentialization enables framing all generation tasks as next-token prediction problems, thereby harnessing the scalability and flexibility inherent in autoregressive models for scientific applications. And we will show that this approach can handle various tasks across different scientific domains.

Figure 1 depicts our sequentialization scheme, which unifies symbolic (words) and numerical data (numbers) into a single sequence delineated by special tokens. For small molecules, the `<bos>` token marks the onset of the SMILES string, while `<boc>` signals the commencement of its coordinate sequence. A parallel approach is applied to materials, with `<bof>` initiating the chemical formula and `<boc>` the coordinate sequence. The `<eos>` token is appended to signify the sequence’s termination. This methodology facilitates the encoding of diverse scientific data into a unified sequence format and is adaptable to other data types, including protein and DNA sequences. The explanation of the special tokens is provided in the Table S9.

This sequentialization method offers a simple and effective way to represent diverse scientific data across various domains and tasks. However, traditional sequence models struggle to handle numerical data (numbers) with the same efficacy as symbolic data (words), particularly when numerical precision is crucial. A diffusion strategy combined with a sequence model effectively handles both numerical and symbolic data within a sequence modeling framework. This approach will be detailed in the following subsection.

2.2 Bridge the Gap: Unified Sequence Modeling of Words and Numbers

The key principle of this design is “word-to-word, number-to-number” prediction. Specifically, a causal attention transformer decoder (AR module) performs next-token prediction. If the predicted token is a word, a standard cross-entropy loss is computed. In contrast, if the predicted token represents a number, the diffusion head is activated to predict the diffusion target conditioned on the output of AR module, and a diffusion loss is calculated. To improve training efficiency, losses from several diffusion time steps are aggregated and combined with the word loss to jointly train the transformer decoder and the diffusion head. This process is illustrated in Figure 2(a), where the sequence “`<bos>CHHHI<boc>coordinates`” (a mixture of words and numbers) is fed into the AR module for next-token prediction using causal attention. Finally, the total loss, computed as the sum of the word loss and the aggregated diffusion loss, is used to jointly train the AR module and the diffusion head (Figure 2(b)). To fully leverage the conditioning h from the autoregressive next-token prediction, we sample multiple diffusion time steps t_1, t_2, \dots, t_M for the diffusion head and sum the corresponding M diffusion losses to obtain the final diffusion loss (Figure 2(c)).

This design treats words and numbers equally within the autoregressive framework but employs distinct heads to model the discrete and continuous spaces, respectively. The majority of parameters reside within the autoregressive module, responsible for next-token prediction, while the diffusion head is significantly lighter. This is because the autoregressive module captures most of the contextual information in the predicted token, leaving only a low-dimensional variable for the diffusion process. This approach differs substantially from traditional joint diffusion training and consequently requires far fewer parameters and time steps for training the diffusion head. The diffusion head operates on a single variable at a time, for example, the three-dimensional coordinates or forces of a specific atom. Consequently, the diffusion training is agnostic to the semantic meaning of the variable; whether it represents coordinates, energy, or force is irrelevant to the diffusion process

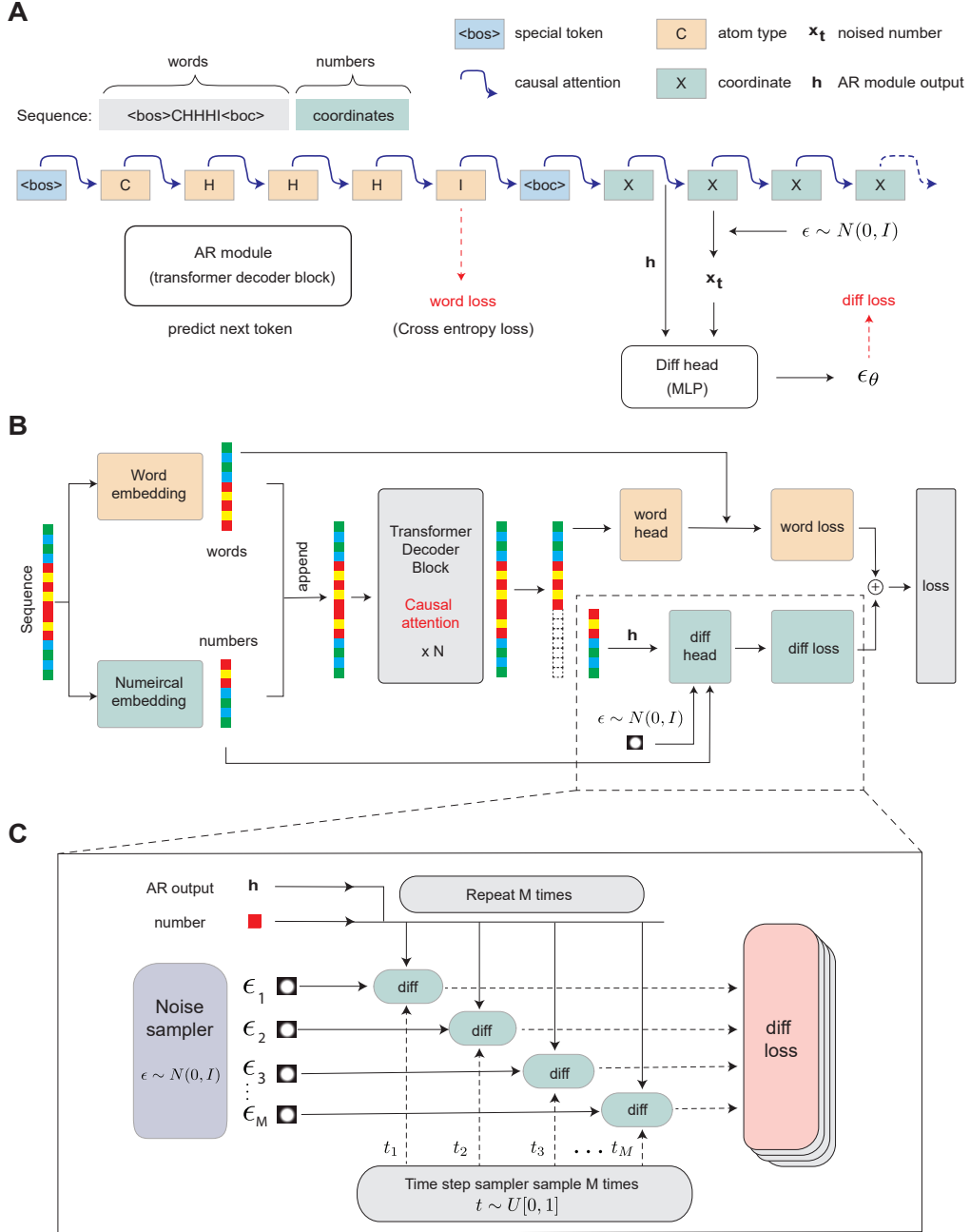


Figure 2: The scheme of the UniGenX framework for a unified generation. We present a novel autoregressive diffusion framework for science generation, surpassing traditional LLMs and structural prediction models. By combining next-token prediction and conditional diffusion, our approach offers enhanced flexibility, overcomes the difficulties of training of the traditional jointly diffusion, and the numerical accuracy issues that have limited the application of LLMs in high-precision scientific fields.

itself. Therefore, a single diffusion head can be used for training all numerical data without loss of precision. Therefore, our model exhibits significant flexibility across diverse domains and tasks that can be represented as sequences of words and numbers.

Our model does not incorporate explicit inductive biases for equivariance or invariance. This design choice grants significant flexibility in handling diverse tasks and scientific domains with varying symmetry requirements. We demonstrate through our results that learning specific equivariant or invariant properties can be effectively achieved through data augmentation, thus preserving the scalability of the underlying transformer architecture.

Remark 1. Benefits of Unified training of Sequence and Structure. *Beyond the advantages for generation capabilities derived from the unified generation of sequence and structure, we emphasize the training perspective. Unified training allows the model to more comprehensively capture the inherent knowledge within scientific data. To illustrate, let s denote the sequence, x the coordinates of the structure, and f_θ the model with training parameters θ . The learned mappings for different models are as follows:*

$$\begin{cases} f_\theta^{\text{diffusion}} : s \mapsto x, & \text{Sequence-to-structure diffusion models,} \\ f_\theta^{\text{sequence}} : s \mapsto s, & \text{Sequence-to-sequence autoregressive models,} \\ f_\theta^{\text{UniGenX}} : (s, x) \mapsto (s, x), & \text{UniGenX model.} \end{cases}$$

The joint mapping $f_\theta^{\text{UniGenX}}$ from (s, x) to (s, x) significantly enhances knowledge distillation from scientific data compared to the other two mappings. In scientific domains, the properties or functions of a molecule are determined by both its sequence and structural coordinates, which are richly interconnected. The joint training strategy enables UniGenX to uncover these interdependencies, leading to improved performance in understanding and generation tasks. Consider the co-evolution of amino acids in a protein for example: two amino acids, though not adjacent in the sequence, may be spatially close in the 3D structure. Consequently, a mutation in one amino acid can induce a related mutation in the other. A sequence-only model would entirely miss this information, and a sequence-to-structure model, while capturing some information from extensive sequence-structure data, lacks explicit sequence modeling due to the absence of a sequence-based loss.

3 Experiments

To evaluate UniGenX, we conduct experiments across various tasks in the materials and small molecule domains. In this work, we present two model configurations of different sizes: UniGenX(100M) and UniGenX(400M), where the transformer decoder backbones contain 100M and 400M parameters, respectively. See Table S5 for detailed model configurations. In general, UniGenX(400M) outperforms UniGenX(100M) reflecting scaling law in this model architecture.

3.1 Material

For material domain, we evaluate UniGenX on crystal structure prediction and de novo generation task.

3.1.1 Crystal Structure Prediction

In this task, we performed finetuning and evaluations on three mainstream benchmarks. The MP-20 dataset is a subset of the Materials Project [13]. It encompasses all materials with a unit cell atomic

count less than 20, and most properties can achieve DFT accuracy. Carbon-24 [14] contains 10k carbon materials, which share the same composition, but have different structures. Similar to the MP-20 dataset, it covers materials composed only of carbon atoms with a unit cell atomic count less than 24. The MPTS-52 dataset includes time-based splits for cross-validation and benchmarking generative models, allowing up to 52 atoms in the unit cells.

The performance is compared with three baselines in Table 1 which are all previous state-of-the-art methods. Notably, In contrast to them, our model does not incorporate explicit inductive biases for equivariance or invariance, we demonstrate through our results that these properties can be effectively learned through data augmentation, preserving the scalability of the underlying transformer architecture and providing flexibility across diverse tasks and scientific domains with varying symmetry requirements. CDVAE [15] is modified in [9] to perform the CSP task by replacing its original normal prior for generation with a parametric prior conditioned on the encoding of the specified composition.

Method	Model Type
CDVAE[15](modified by [9])	Variational Autoencoder (VAE)
DiffCSP[9]	Diffusion Model
FlowMM[10]	Riemannian Flow Matching

Table 1: Comparison of generative models for crystal structure prediction.

We pretrained our model on a comprehensive dataset that we constructed, which includes the training sets of MP-20, Carbon-24, MPTS-52 ,and a subset of data from NOMAD, which are disjoint from all test sets. Subsequently, we finetuned the pretrained model on MP-20, Carbon-24, and MPTS-52 respectively. For evaluation, following [15], we employed **StructureMatcher** [16] to compute metrics including the Match Rate and the Root-Mean-Square Derivation (RMSD) with thresholds $\text{stol}=0.5\text{\AA}$, $\text{angle_tol}=10^\circ$, $\text{ltol}=0.3\text{\AA}$. The Match Rate represents the percentage of matched structures within the test set. The RMSD is computed between the ground truth and the matched structure.

3.1.2 De Novo Generation

As a unified model, UniGenX inherently possesses the capability of de novo generation. Following [10], we let the model finetuned on MP-20 generate 10,000 materials. Different from CSP task, It start with only begin token **<bos>** and generating the compositions and structures through sampling and diffusion.

We assess the generation performance using three metrics: Validity, Coverage, and Property Statistics. Validity measures the correctness of the predicted crystals. Coverage evaluates the similarity between the test set and the generated samples. Property Statistics calculates properties such as density and the number of elements.

3.1.3 Conditional Generation

As an autoregressive model, one of its key features is the ability to perform controllable conditional generation with ease. Therefore, we evaluate UniGenX on conditional generation tasks, where the goal is to generate stable crystal structures that satisfy specific target conditions. This setting reflects real-world design scenarios in which materials are sought with desired physical or chemical properties.

To enable conditional generation, we prepend a special token to the input sequence, which includes both the material composition and structure, to indicate the target property type. Sequentially, we embed the target property value using a multilayer perceptron (MLP) and append it to the sequence, in front of the material’s composition and structure. We finetune our pretrained model using datasets with property labels. We focus on scalar property conditioning, targeting single-valued material properties such as magnetic density and bulk modulus. For each property, we train a separate model using a small-to-moderate-sized labeled dataset.

During training, we apply the loss only on the material itself, without directly supervising the property value. To better handle the numerical range of the target properties, we apply a nonlinear transformation of the form $\text{sign}(x) \cdot \log(|x| + 1)$ to the property values before embedding.

To demonstrate our model’s ability to generate out-of-distribution (OOD) samples, following [17], we consider two scalar property targets:

- **Magnetic Density:** We finetune on 600k structures labeled with magnetic density (in \AA^{-3}), and generate samples targeting values equal to 0.20 \AA^{-3} .
- **Bulk Modulus:** We finetune on a small dataset of 5k samples, targeting high-stiffness materials with a bulk modulus equal to 400 GPa.

During inference, inspired by [18], we employed an earlier checkpoint of our own model—trained for fewer steps—to guide the generation process of the final model. This approach serves as a substitute for the standard classifier-free guidance (CFG), effectively enabling a form of “temperature reduction” during sampling. For the generated materials, property values were evaluated using the MatterSim [19].

3.1.4 Multi-conditional Generation

We further evaluated UniGenX under multi-conditional generation, where the target is to generate materials satisfying multiple properties simultaneously. This is a classic materials design problem involving trade-offs between multiple physical properties. The core significance of this task lies in the fact that these three properties are typically in conflict with one another, making simultaneous optimization highly challenging—providing an ideal benchmark to evaluate the capability of a material generation model. Ultimately, these materials can potentially provide implications in many high-value engineering applications such as aerospace materials, thermal energy storage and management materials, and protective materials etc.

In this setting, we prepend three special tokens to the input sequence, each indicating a specific property type: heat capacity at 300 K (J/g·K), Hill’s elastic modulus(GPa), and density (kg/m^3), followed by their corresponding signed-log-transformed values.

Training and inference procedures remain consistent with the single-condition setup, including the use of classifier-free guidance during sampling.

The multi-labeled dataset is constructed from the Materials Project containing no more than 16 atoms, and employed the pre-trained MatterSim-v1.0.0-5M machine-learning interatomic potential via the ASE and Phonopy interfaces to compute, under the harmonic approximation, each crystal’s Hill’s elastic modulus, its thermal conductivity at 300 K, and its density—these quantities serving as the training labels. For each data item containing three distinct labels, we partition it into $C_3^1 + C_3^2 + C_3^3$ subsets, where each subset contains 1, 2, or 3 labels, respectively. These subsets are then used to fine-tune our model. This strategy is designed to enable UniGenX to flexibly generate structures under varying numbers of conditioning labels, thereby enhancing its versatility in both under- and fully-conditioned generation scenarios.

As a representative multi-conditional generation task, we aim to generate crystal structures that satisfy the following target properties: density of $2.5 \pm 0.2 \text{ kg/m}^3$, Hill’s elastic modulus $E > 200 \text{ GPa}$, and specific heat capacity $C_v > 1 \text{ J/g}\cdot\text{K}$.

3.2 Molecule

For small molecule domain, we evaluate UniGenX on conformation generation and conditional generation tasks.

3.2.1 Conformation Generation

Adopting the data splits defined by DMCG [20], we conducted training and evaluation on the large-scale GEOM-QM9 and GEOM-Drugs datasets. The GEOM dataset [21] comprises three-dimensional conformations for over 37 million molecules, each annotated with experimental data and high-precision Density Functional Theory (DFT) energy values. GEOM-QM9 and GEOM-Drugs are subsets of this comprehensive dataset. Notably, GEOM-QM9 offers a richer conformational diversity compared to the traditional QM9 dataset [22], incorporating intermediate states in addition to ground states, which is advantageous for downstream tasks such as molecular and protein-molecule docking.

Among the comparative methods, GEOMOL [23] employs message passing neural networks (MPNNs) and SE(3)-invariance to predict local atomic 3D structures and torsion angles, facilitating deterministic assembly of complete conformers. ConfGF [24] is a gradient-based model that optimizes molecular 3D structures by learning interatomic distance gradient fields and utilizing score matching for training. DMCG [20], the current state-of-the-art, directly predicts atomic 3D coordinates through a rotation, translation, and permutation-invariant loss function and an iterative refinement architecture.

For evaluation, given molecule x with N_x conformations in the test set, we generate $2N_x$ conformations, following [24]. Let \mathbb{S}_g and \mathbb{S}_r represent the sets of generated and ground truth conformations, respectively. Conformation deviation is quantified using `GetBestRMS` from the `RDKit` package, with root-mean-square deviation denoted as $\text{RMSD}(R, \hat{R})$. The recall-based coverage (COV) and matching (MAT) scores are defined as follows:

$$\text{COV}(\mathbb{S}_g, \mathbb{S}_r) = \frac{1}{|\mathbb{S}_r|} |\{R \in \mathbb{S}_r | \text{RMSD}(R, \hat{R}) < \delta, \exists \hat{R} \in \mathbb{S}_g\}| \quad (1)$$

$$\text{MAT}(\mathbb{S}_g, \mathbb{S}_r) = \frac{1}{|\mathbb{S}_r|} \sum_{R \in \mathbb{S}_r} \min_{\hat{R} \in \mathbb{S}_g} \text{RMSD}(R, \hat{R}) \quad (2)$$

An effective method should exhibit a high coverage (COV) score and a low matching (MAT) score. Following [24, 25], the thresholds (δ) are set to 0.5\AA and 1.25\AA for GEOM-QM9 and GEOM-Drugs, respectively. Precision-based COV and MAT scores are also computed by interchanging \mathbb{S}_g and \mathbb{S}_r in equations 1 and 2. The precision-based coverage and matching scores are defined as follows:

$$\text{COV-P}(\mathbb{S}_g, \mathbb{S}_r) = \frac{1}{|\mathbb{S}_g|} |\{\hat{R} \in \mathbb{S}_g | \text{RMSD}(R, \hat{R}) < \delta, \exists R \in \mathbb{S}_r\}| \quad (3)$$

$$\text{MAT-P}(\mathbb{S}_g, \mathbb{S}_r) = \frac{1}{|\mathbb{S}_g|} \sum_{\hat{R} \in \mathbb{S}_g} \min_{R \in \mathbb{S}_r} \text{RMSD}(R, \hat{R}) \quad (4)$$

3.2.2 Property Evaluation

We extended our evaluation to include molecular property prediction alongside conformation generation, a task that involves predicting properties from generated conformations [21]. Following [20], we randomly selected 30 molecular SMILES from the test set of the GEOM-QM9 dataset. For each molecule, we generated 50 distinct conformations. Using the Psi4 quantum chemistry software package [26], we calculated energy levels, HOMO, and LUMO characteristics for both generated and reference conformations. We then derived ensemble averages for energy (\overline{E}), minimum energy (E_{\min}), average HOMO-LUMO gap ($\Delta\overline{\epsilon}$), and the gap extremities ($\Delta\epsilon_{\min}$ and $\Delta\epsilon_{\max}$) based on the conformational attributes of each molecule. Mean absolute error (MAE) was used to quantify property discrepancies between generated and reference conformations. Given our model’s superior performance in predicting these statistical quantities, depicted in Sec. 4.2, such as average energy and average HOMO-LUMO gap, we further compared the distribution of sampled results from UniGenX with the ground-truth conformations.

3.2.3 Conditional Generation

We further explored our model’s conditional generation capabilities. Instead of employing guidance in the diffusion model, UniGenX utilizes a straightforward approach: prepending the training data sequence with the condition property and its value, marked by a special token like <bobulk> for the bulk property. This enables simple prompting at inference, where conditional generation is achieved by providing the property-value pair and the sequence generation special token. Data processing examples are detailed in Appendix C.5. In this section, using conditional molecule generation on the QM9 benchmark as an example, we demonstrate UniGenX’s strong performance and note its easy extensibility to different domains.

Following [27], the QM9 dataset is divided into two halves, the first half is used to train the classifier, while the second half is used to train our model. For the classifier, we use the training weights provided by [28] to achieve a fair comparison. Unlike other diffusion models, we wrap the condition into the sequence. Only one special token is needed for wrapping. Refer to Appendix for more details.

The properties include volume $\alpha(\text{Bohr}^3)$, the ability of a molecule to become polarized under an external electric field; HOMO $\epsilon_H(\text{meV})$, the energy level of the highest occupied molecular orbital; LUMO $\epsilon_L(\text{meV})$, the lowest unoccupied molecular orbital energy; energy gap $\Delta\epsilon(\text{meV})$, the energy difference between HOMO and LUMO; dipole moment $\mu(D)$, the separation of positive and negative charges within the molecule.

For evaluation, we employed two different sampling methods. The first, introduced in [27], models the distribution of conditions in the training set based on equation 6. It first samples the number of atoms, N , and then samples the property values corresponding to N . The second method, proposed by [28], addresses a potential inductive bias in the original method from [27], where an implicit correlation between molecule size and properties may arise during evaluation. To mitigate this, they propose uniformly sampling property values directly between the minimum and maximum values, as described in equation 5.

We evaluated our model’s performance aligning both sampling methods. Notably, unlike prior approaches that trained separate models for each property and relied on extensive preprocessing, our model is trained as a unified, all-in-one model and not require pre-generation of the number of atoms, N .

$$p(\mathcal{M}|\mathbf{x}_{\text{cond}}) \propto \sum_N p(\mathcal{M}_N|N, \mathbf{x}_{\text{cond}})p(N) \quad (5)$$

$$p(\mathcal{M}|\mathbf{x}_{\text{cond}}) \propto \sum_N p(\mathcal{M}_N|N, \mathbf{x}_{\text{cond}})p(N)p(\mathbf{x}_{\text{cond}}|N) \quad (6)$$

3.2.4 Multi-conditional Generation

In the domain of small molecule conditional generation, another crucial task is multi-condition generation. Since our model is a sequence model, it easily accommodates multiple condition properties by appending them to the beginning of the sequence for conditional generation.

We have observed that previous works typically focus on single-condition generation and train models using only one condition. Here, we introduce a multi-condition generation setting. Consistent with [27], we divide the QM9 dataset equally into two halves, with the first half used to train the classifier and the second half to train our model. The QM9 dataset contains six comparable properties, so we select n properties (where $1 \leq n \leq 6$) for splitting the data. This results in a total of $\binom{6}{1} + \binom{6}{2} + \binom{6}{3} + \binom{6}{4} + \binom{6}{5} + \binom{6}{6} = 63$ data splits. We continue to use the training weights provided by [28] for our classifier. Similar to single-condition generation, we embed conditions into the sequence, requiring only one special token per condition for embedding. For multi-condition generation, we determine the order of conditions based on the sorted string representation of them.

During the evaluation phase, we randomly selected 1k values from any of the 63 condition combinations in the divided test set for generation, and subsequently assessed them using a classifier. We believe that calculating the Mean Absolute Error (MAE) for each property in multi-condition generation lacks significant meaning. The primary focus is for our generator to produce distributions that meet real-world requirements. Therefore, for different condition combinations, we plotted the distribution of both the actual data and the generated data.

3.3 Protein

We pre-trained a 400M-parameter model using approximately 78 million protein sequence–structure pairs from the AFDB. These proteins were selected based on sequence identity below 90% and pLDDT scores above 70. During training, sequences longer than 256 residues were randomly truncated, enabling the model to effectively learn the relationship between protein sequences and their 3D structures, and to support downstream tasks.

3.3.1 Emulating MD equilibrium distributions

We evaluated UniGenX’s ability to model long-timescale molecular dynamics (MD) equilibrium distributions using simulations of 12 fast-folding proteins generated by [29] on the special-purpose supercomputer Anton.

From the DESRES fast-folding MD trajectories, we sampled one snapshot every 10 frames to construct the dataset. For each snapshot, we extracted the Cartesian coordinates of the alpha carbon atoms ($C\alpha$) as a representation of the amino acid positions, along with the corresponding one-letter amino acid sequence. To mitigate overfitting, we incorporated a 5% subset of the AFDB training data containing sequences shorter than 80 residues into the training set.

We then trained 12 “DESRES-finetuned models,” each fine-tuned on 11 fast folders using our base model pretrained on AFDB data, and tested on the remaining held-out fast folder. Across these 12 tasks, our model successfully recovered native and unfolded states that are structurally consistent with the expected free energy landscapes of the proteins.

For evaluation, we employed Time-lagged Independent Component Analysis (TICA) to identify low-dimensional projections associated with the system’s slowest dynamical processes. Using pairwise distance matrices of protein structures as input, TICA extracts directions corresponding to the most kinetically relevant degrees of freedom, which effectively serve as latent axes of the free energy landscape. We then projected the trajectories onto the first two TICA components to visualize the system in a 2D plane, where each point represents a protein conformation. High-density regions in this space correspond to low free energy (i.e., highly probable) states, while sparse regions indicate high free energy (i.e., less probable) states. This analysis enables us to assess whether UniGenX has successfully learned to reproduce the true long-timescale MD equilibrium distributions.

3.3.2 EC Number-guided Protein Generation

The Enzyme Commission (EC) number is a numerical classification scheme for enzymes based on the chemical reactions they catalyze. Each EC number consists of four hierarchical levels (e.g., 2.6.1.1), providing increasingly specific information about enzyme function. In our work, we use only the first three levels (e.g., 2.6.1) as generation conditions, which is sufficient to define the primary functional class of the target enzyme while maintaining generalization.

Our approach to EC number-guided protein generation follows the same design as the molecular and material property-conditional generation described earlier. Specifically, the EC number is converted into a sequence of tokens and special tokens, which are prepended to the input sequence. For example, an EC number 2.6.1.x is encoded as `<ec1>2<ec2>6<ec3>1<prot>` at the beginning of the input sequence and structure tokens.

For training data, we used all protein sequences in UniProt that have an assigned EC number and corresponding structural information available in the AlphaFold Database (AFDB), and with sequence lengths below 512 residues. This results in a dataset of approximately 20 million samples.

To evaluate the effectiveness of EC number conditioning, we selected three representative EC numbers and generated 400 protein sequences for each. The validity of the generated sequences was first checked using CLEAN [30] to ensure they conformed to the assigned EC number. To further assess the structural quality and functional relevance, we predicted the 3D structures of the generated sequences using ESMFold [31], performed sequence alignment against the UniProt database using BLAST, and conducted structural comparisons against AFDB and PDB using Foldseek [32]. Additionally, to evaluate the contribution of structure information during training, we trained a sequence-only version of the model as a baseline for comparison.

3.4 Protein-Ligand Docking

A central challenge in structural biology is the accurate prediction of small-molecule ligands that bind to a given protein pocket [33]. Most existing approaches rely on static, co-crystallized protein-ligand complexes, failing to account for the conformational flexibility that proteins often exhibit upon ligand binding. In this work, we formulate two related tasks that explicitly incorporate protein dynamics into the modeling process.

The first task involves predicting the bound ligand conformation given both the unbound (apo) and bound (holo) pocket structures. The second, more challenging task requires predicting both the holo pocket conformation and the bound ligand coordinates from the apo structure alone. Together, these tasks aim to model the dynamic nature of molecular recognition and capture induced-fit effects that are often neglected in traditional structure-based docking pipelines. To this end, we leverage the MISATO dataset [34], which comprises approximately 20,000 experimentally resolved protein-ligand

complexes along with over 170 microseconds of molecular dynamics (MD) trajectories—offering a unique view into the conformational transitions involved in binding events.

To construct inputs for these tasks, we use AlphaFold2-predicted structures[35] as proxies for the unbound (apo) state of proteins. Because the MISATO dataset does not retain original chain identifiers and includes preprocessing steps such as hydrogen addition, we use the PDBbind dataset[36] as a reference. We first align each MISATO complex to its corresponding entry in PDBbind, then align the relevant chains to their AlphaFold2-predicted structures from the AlphaFold Protein Structure Database (AFDB) using UniProt identifiers. This two-step alignment allows us to establish residue-level correspondences between experimental and predicted structures. Binding pockets are subsequently extracted using the MISATO-provided script, which selects all residues within 10 Å of the ligand.

Following this preprocessing pipeline, we obtain 9,744 protein-ligand complexes, each with 100 MD snapshots. We adopt the CASF-2016 benchmark split[37] to partition the data into 9,587 training samples and 157 test samples. Each small molecule is represented using its canonical SMILES string after hydrogen removal, while protein pockets are represented at the all-atom level.

Each test sample is evaluated using $2N_f = 200$ generated conformational frames. The two prediction tasks are assessed using distinct evaluation protocols. In the ligand-only prediction task, where both apo and holo pocket structures are provided as input, performance is measured by computing the root-mean-square deviation (RMSD) between the predicted ligand coordinates and the ground truth ligand in the corresponding MD frame. In the joint prediction task, which requires generating both the holo pocket and the ligand from the apo structure alone, evaluation is conducted separately for the ligand, the pocket, and the full protein-ligand complex. For each of these components, RMSD is computed against all MD frames corresponding to the same PDB ID, and the minimum RMSD across frames is reported. This flexible evaluation accounts for the conformational ambiguity inherent in dynamic binding processes, recognizing that multiple structurally distinct solutions may be equally valid.

3.5 Unification training on Material and Molecule

We demonstrated our model’s ability to perform unified training and generation across diverse scientific domains. Specifically, we trained a single model on both molecule and material datasets. As detailed in the methods, UniGenX not only accommodates pure sequences, such as crystal formulas in materials or SMILES strings in small molecules, but also effectively handles numerical tokens, such as atomic coordinates, through its diffusion heads. This showcases UniGenX’s potential for unifying various scientific domains by training a single model across different tasks and datasets.

To differentiate domains, we introduced special tokens for materials and molecules as indicators during training. We trained a 100M parameter model on a combined dataset of 5M material data and 1M QM9 molecule data, denoted as UniGenX(100M). We then finetuned this model on material datasets including MP-20, Carbon-24, and MPTS-52, as well as the 1M GEOM-QM9 molecule dataset.

3.6 Combing with Large Language Model

To facilitate more effective integration with the LLM, we performed two tasks: (1) fine-tuning the language model to endow it with the capability of predicting crystal structures; and (2) incorporating a gating module that enables the model to dynamically switch between generating textual and numerical outputs.

Building upon our approach, which leverages an autoregressive sequence model backbone and joint training on symbolic and numerical data, UniGenX naturally lends itself to language capabilities. We explored this by loading a pretrained language model and performing instruction tuning on the structure prediction task using language prompts. For example, The MP-20 dataset was reconstructed into an instruction tuning dataset, with the data format detailed in Appendix C.10.

To enable the model to seamlessly switch between generating textual and numerical outputs — such as producing a set of structural coordinates followed by explanatory text — it is crucial for the model to autonomously predict whether the feature vector should be routed through the lm head or the diffusion head prior to entering them, rather than relying on this information as a given.

For this purpose, we introduced a gating module shown in Figure 4 that performs a binary classification on the model’s final hidden state to determine which head it should pass through.

We then finetuned the pretrained model, which had approximately 1B parameters from NatureLM [38], on MP-20 and QM9, demonstrating its superior performance.

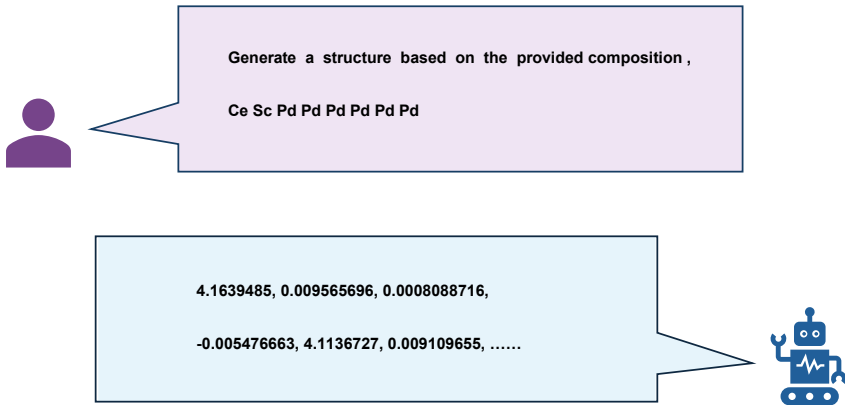


Figure 3: An example for instruction tuning for the Crystal Structure Prediction (CSP) task.

4 Results

We evaluated UniGenX on crystal structure prediction and de novo generation in the material domain, conformation generation and conditional generation in the molecular domain, unification and language capacity.

4.1 Material Results

The evaluation metrics are summarized in Table 2 and Table 3 for baseline methods and our model in Crystal Structure Prediction and de novo generation, respectively. As shown in Table 2, our model significantly outperforms the previous diffusion/flow matching state-of-the-art, FlowMM, achieving match rate increases of **10%**, **28%**, and **120%** on MP-20, Carbon-24, and MPTS-52, respectively. In terms of RMSD, we observe improvements of **35%**, **45%**, and **62%**. Compared to NatureLM [38], a recently published autoregressive model that surpassed FlowMM on the MP-20 and MPTS-52

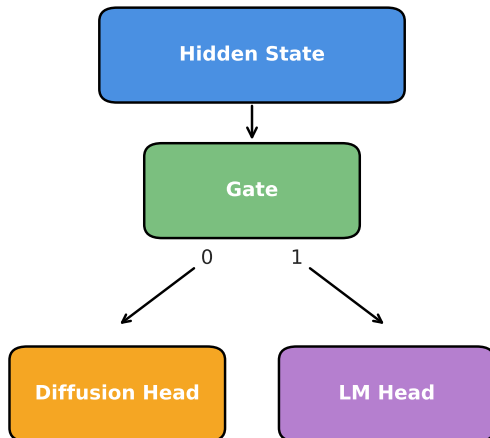


Figure 4: Diagram of the hidden state, gate, and heads.

	MP-20		Carbon-24		MPTS-52	
Methods	MR(%) \uparrow	RMSD(\AA) \downarrow	MR(%) \uparrow	RMSD(\AA) \downarrow	MR(%) \uparrow	RMSD(\AA) \downarrow
CDVAE[15]	33.90	0.1045	17.09	0.2969	5.34	0.2106
DiffCSP[9]	51.49	0.063	17.54	0.2759	12.19	0.1786
FlowMM[10]	61.39	0.057	23.47	0.4122	17.54	0.1726
NatureLM[38]	61.78	0.044	–	–	30.20	0.084
UniGenX(400M)	67.01	0.037	30.05	0.2286	38.65	0.0657

Table 2: Crystal structure prediction results on material benchmarks. “-” indicates unreported results. Compared to the latest, our model achieves a 10% improvement in match rate on MP-20, and a 28% improvement on Carbon-24 and MPTS-52. Our model significantly outperforms the state-of-the-art, with increased performance on longer sequences(materials with larger unit cells).

Methods	InSteps	VS (%) \uparrow	VC (%) \uparrow	CR (%) \uparrow	CP(%) \uparrow	PW(ρ) \downarrow	PW(Nel) \downarrow
CDVAE[15]	5000	100	86.7	99.15	99.49	0.688	0.278
DiffCSP[9]	1000	100	83.25	99.71	99.76	0.35	0.125
FlowMM[10]	250	96.58	83.47	99.48	99.65	0.261	0.107
FlowMM[10]	1000	96.85	83.19	99.49	99.58	0.239	0.083
UniGenX(100M)	200	99.08	90.12	99.27	99.95	0.065	0.04

Table 3: De novo generation tasks benchmark. The abbreviations in the table refer to: Integration steps(InSteps), Validity Structural(VS), Validity Composition(VC), Coverage Recall(CR), Coverage Precision(CP) and Property Wdist(PW).

benchmarks, our model also demonstrates superior performance, establishing a new state-of-the-art across MP-20, Carbon-24, and MPTS-52.

The significant improvement on MPTS-52 is particularly noteworthy. We speculate that this is due to our model’s inherent long-range perception capabilities, a feature often lacking in graph-based representations. The results in Table 2, compared with both diffusion/flow matching and autoregressive models, underscore the importance and effectiveness of combining diffusion and autoregressive models in our approach.

Table 3 shows that UniGenX can generate materials attributed to more reasonable, more precise, and more realistic under the condition of fewer steps. Specifically, on the Property Wdist metric, which is an index on which previous models did not perform well, UniGenX can achieve scores of 0.065 for ρ (density) and 0.04 for Nel (number of electrons) in just 200 steps. Compared to the previously most advanced model, this represents an improvement of **73%** and **52%**, respectively.

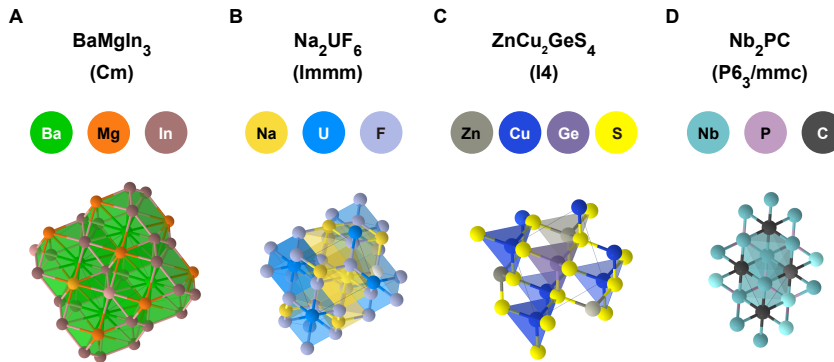


Figure 5: Examples of generated material structures from the crystal structure prediction task. The generated structures closely resemble the ground truth structures; therefore, the latter are omitted for clarity and conciseness.

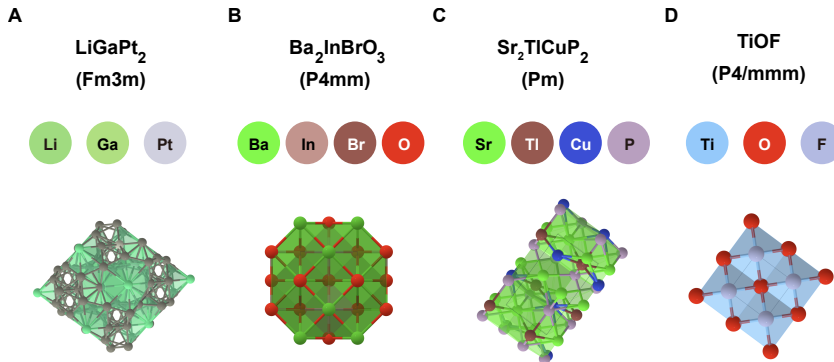


Figure 6: Examples of generated material structure in de novo generation task

Some examples of crystal structure prediction results are shown in Figure 5, and Figure 6 displays

some examples of de novo generation, in terms of both material formula and crystal structures.

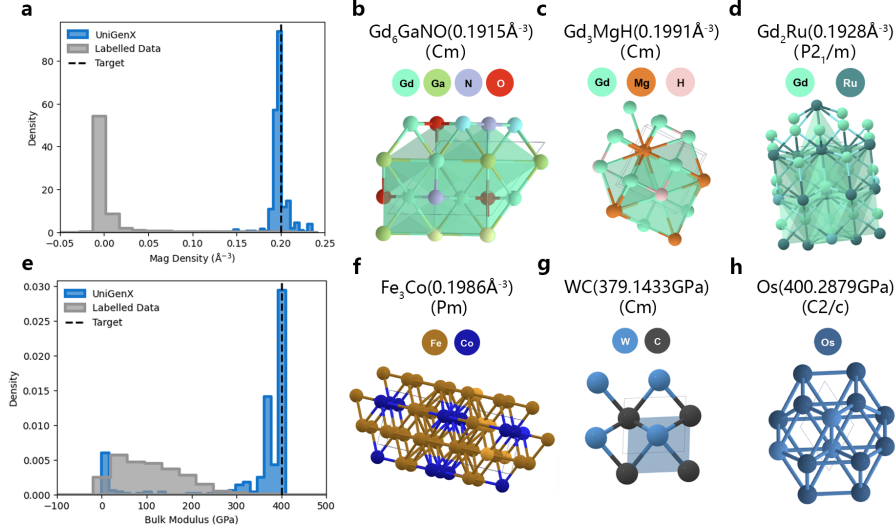


Figure 7: Generated materials with target magnetic and mechanical properties. Panels (a) and (e) show the density distributions of the target properties for the stable samples generated by UniGenX, alongside the corresponding label distributions in the fine-tuning dataset for magnetic (a) and mechanical (e) properties. The target value specified for UniGenX is indicated by a black dashed line. Panels (b-d) and (f-h) visualize representative S.U.N. structures generated under magnetic (b-d) and mechanical (f-h) property conditions, each annotated with the reduced formula, space group, and the predicted property value. The model demonstrates the ability to generate samples beyond the support of the training data, particularly in out-of-distribution (OOD) regions, highlighting its strong generalization capability.

Figure 7 presents the results of the material generation task conditioned on a single property. Panels (a) and (e) show the density distributions of the target properties for the stable samples generated by UniGenX, alongside the corresponding label distributions in the fine-tuning dataset for magnetic (a) and mechanical (e) properties. The target value specified for UniGenX is indicated by a black dashed line. Panels (b-d) and (f-h) visualize representative S.U.N. structures generated under magnetic (b-d) and mechanical (f-h) property conditions, each annotated with the reduced formula, space group, and the predicted property value. Notably, UniGenX demonstrates the ability to generate samples beyond the support of the training data, particularly in out-of-distribution (OOD) regions. This highlights the model’s strong generalization capability—its ability to push forward from one distribution to another.

During experiments, we observed that the temperature and top-p value of UniGenX have a significant impact on the quality of material generation. Higher temperature and top-p values lead to increased diversity among generated samples and a greater proportion of novel materials. In contrast, lower values result in property distributions that are more sharply concentrated around the target. Under the optimal setting, UniGenX achieves an inference speed of 0.315 seconds per S.U.N. structure, demonstrating its practical efficiency for structural generation.

Figure 8 illustrates the performance of UniGenX on the task of multi-property-constrained material generation. In panel (a), gray dots represent the distribution of labeled training data, while

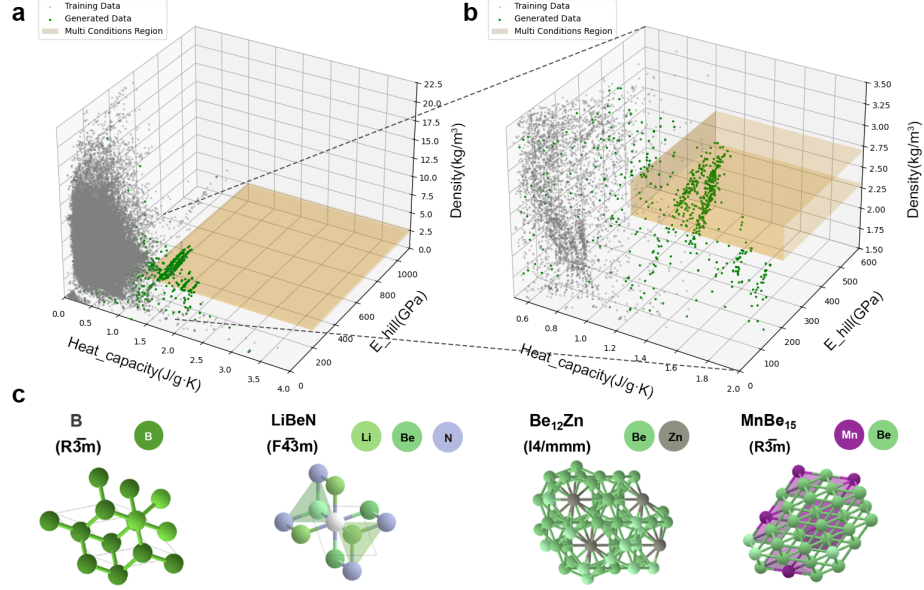


Figure 8: Generating materials with multi-objective constraints. This figure illustrates the performance of UniGenX on the task of material generation under multiple property constraints. In panel (a), gray dots represent the distribution of labeled training data, while green dots denote the distribution of samples generated by our model. The yellow-shaded region indicates the domain defined by the target constraints for this task ($2.3 \text{ g/cm}^3 \leq \text{density} \leq 2.7 \text{ g/cm}^3$, heat capacity $> 1 \text{ J/g}\cdot\text{K}$, $E_{\text{Hill}} > 200 \text{ GPa}$). Panel (b) provides a detailed view of how the generated samples populate the constrained property space. Panel (c) presents selected examples of SUN (Stable, Unique, and Novel) structures among the generated samples. Out of 1,262 generated candidates, our model successfully identified 436 stable structures that satisfy all specified property constraints. Four of these were confirmed by DFT to be novel, thermodynamically stable compounds not present in existing databases.

green dots denote the distribution of structures generated by our model. The yellow-shaded region defines the desired target domain: $2.3, \text{g/cm}^3 \leq \text{density} \leq 2.7, \text{g/cm}^3$, heat capacity $> 1, \text{J/g}\cdot\text{K}$, and $E_{\text{Hill}} > 200, \text{GPa}$. Panel (b) zooms in on the coverage of the generated samples within this constrained property space, and panel (c) showcases selected SUN structures among the successful generations. Out of 1262 generated candidates, our model identified 436 structures predicted to be both stable and compliant with all target property constraints.

To further evaluate novelty, we conducted a rapid screening procedure based solely on elemental composition, filtering out structures present in the training set. This process yielded 11 novel candidates, of which 4 were confirmed through DFT calculations to satisfy all property requirements while also exhibiting thermodynamic stability. None of these four materials were found in the Materials Project database, suggesting they may represent previously unreported compounds.

Although this screening was intentionally limited in scope for computational efficiency, it demonstrates the model’s ability to generate valid, constraint-satisfying, and potentially novel materials. A more exhaustive comparison across the full set of generated structures would likely uncover additional unique candidates, offering further evidence of UniGenX’s potential in accelerating inverse material design under multi-objective constraints.

4.2 Molecular Results

Dataset	Large-scale QM9				Large-scale Drugs			
Methods	COV-P (%) \uparrow		MAT-P (\AA) \downarrow		COV-P (%) \uparrow		MAT-P (\AA) \downarrow	
	Mean	Median	Mean	Median	Mean	Median	Mean	Median
ConfGF[24]	46.23	44.87	0.5171	0.5133	28.23	20.71	1.6317	1.6155
GeoMol[23]	78.28	81.03	0.3790	0.3861	41.46	36.79	1.5120	1.5107
DMCG[20]	90.86	95.36	0.2305	0.2258	74.57	81.80	0.9940	0.9454
UniGenX(400M)	91.40	100.00	0.2516	0.1070	76.94	87.50	1.3394	0.8631

Table 4: Conformation generation: precision-based coverage and matching score. Our model surpasses the state-of-the-art on most metrics.

Dataset	Large-scale QM9				Large-scale Drugs			
Methods	COV (%) \uparrow		MAT (\AA) \downarrow		COV (%) \uparrow		MAT (\AA) \downarrow	
	Mean	Median	Mean	Median	Mean	Median	Mean	Median
ConfGF[24]	89.21	95.12	0.2809	0.2837	70.92	85.71	1.0940	1.0917
GeoMol[23]	91.05	95.55	0.2970	0.2993	69.74	83.56	1.1110	1.0864
DMCG[20]	98.34	100	0.1486	0.1340	96.22	100.00	0.6967	0.6552
UniGenX(400M)	92.67	100	0.1466	0.0856	92.09	100.00	0.6536	0.6120

Table 5: Conformation generation: Recall-based coverage and matching score

As shown in Table 4 and Table 5, the conformations generated by our model are able to achieve good Coverage and Match score whether based on recall or precision. Overall, the results are comparable to DMCG [20]. It is noticeable that for every metric’s median we outperform the baselines; the remaining ones are only a little lower than DMCG.

The results of property evaluation are shown in Table 6. Our method significantly outperforms SOTA and baseline methods listed in the Table, which shows the effectiveness of our method. Comparison between the distribution of energies and gaps of ground truth and generated conformations is in Figure 9.

Methods	\bar{E}	E_{\min}	$\bar{\Delta\epsilon}$	$\Delta\epsilon_{\min}$	$\Delta\epsilon_{\max}$
RDKit	0.8875	0.6530	0.3484	0.5570	0.2399
ConfGF[24]	2.8349	0.2012	0.6903	4.9221	0.1820
GeoMol[23]	4.5700	0.5096	0.5616	3.5083	0.2650
DMCG[20]	0.4324	0.1364	0.2057	1.3229	0.1509
UniGenX(400M)	0.1464	0.0746	0.1004	0.2241	0.1360

Table 6: Mean absolute error of predicted ensemble properties (Unit: eV)

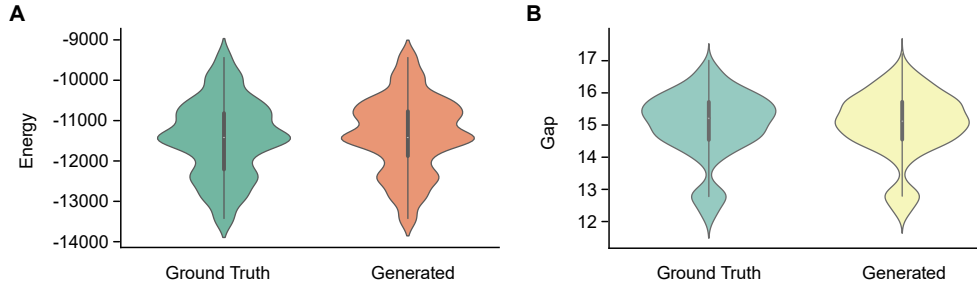


Figure 9: Comparison of energy (A) and gap (B) property distributions between ground truth and generated conformations.

Model	$\alpha(Bohr^3)$	$\epsilon_H(mHa)$	$\epsilon_L(mHa)$	$\Delta\epsilon(mHa)$	$\mu(D)$
Random	41.00	103.30	121.83	193.36	8.40
EDM[27]	20.15	158.70	166.20	287.00	7.01
LDM-3DG[28]	15.56	54.62	63.08	107.14	6.33
LDM-3DG-GSSL[28]	16.43	55.03	66.53	113.15	9.22
DiGress[39]	9.23	31.98	105.06	90.57	1.49
SeaDAG[40]	8.85	30.91	103.03	89.70	1.33
UniGenX(100M)	2.46	18.40	21.47	55.77	0.99

Table 7: Conditional generation on five quantum properties(unit) evaluation following LDM setting in [28]. Numbers represent the MAE between conditional and oracle-predicted properties [41].

Property Units	α Bohr ³	$\Delta\epsilon$ meV	ϵ_{HOMO} meV	ϵ_{LUMO} meV	μ D	C_v $\frac{\text{cal}}{\text{mol}}\text{K}$
QM9	0.10	64	39	36	0.043	0.040
Random	9.01	1470	645	1457	1.616	6.857
EDM[27]	2.76	655	356	584	1.111	1.101
GeoLDM[42]	2.37	587	340	522	1.108	1.025
GeoBFN[43]	2.34	577	328	516	0.998	0.949
Geo2Seq with Mamba[44]	0.46	98	57	71	0.164	0.275
Geo2Seq with GPT[44]	0.53	102	48	53	0.097	0.325
MOL-STRUCTOK[45]	0.33	89	64	62	0.285	0.169
UniGenX(100M)	0.38	65	39	35	0.045	0.194

Table 8: Conditional generation results for five quantum properties (units specified), evaluated using the EDM setting from [27]. Numbers represent the mean absolute error (MAE) between conditional and oracle-predicted properties [41]. The QM9 row indicates the baseline MAE of the EGNN model, used to obtain the oracle-predicted properties for generated samples, compared to QM9 property labels.

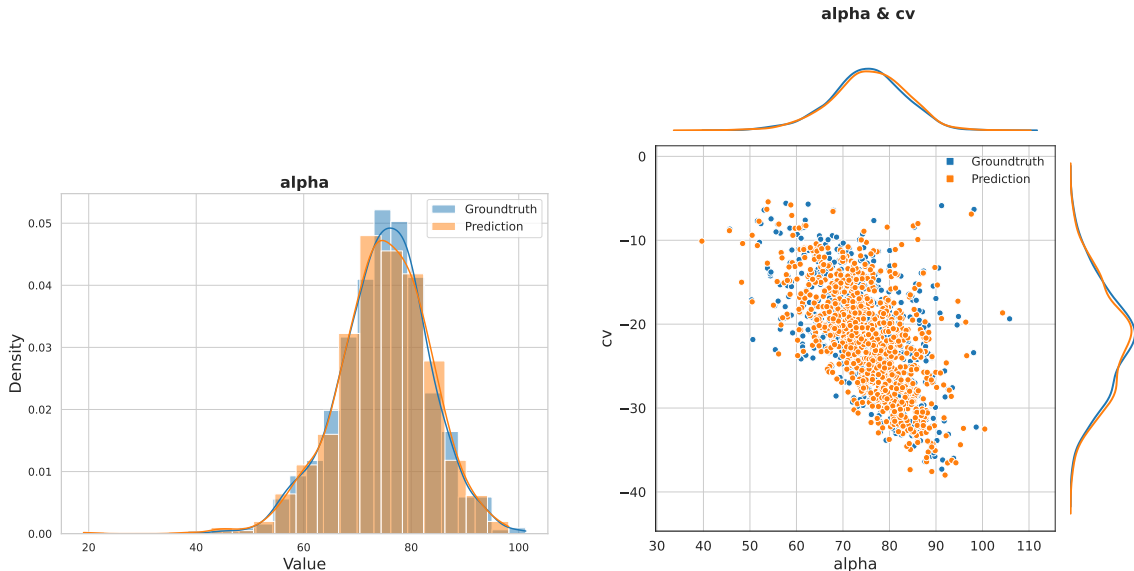
Table 7 presents sampling results according to equation 5 for conditional generation as introduced in [28], where UniGenX achieves state-of-the-art (SOTA) performance across all five properties. Compared with the latest state-of-the-art methods, UniGenX achieves up to a 260% improvement and at least a 34% improvement across various evaluation metrics.

Remark 2. *Corrected the typo from meV to Ha in Table 7. There is a typo with the evaluation results provided by [28]. Following [27], when we used another portion of the QM9 dataset to assess the performance of the classifier from [28], we found that the values for ϵ_H , ϵ_L and $\Delta\epsilon$ were approximately 27.21 times larger than those reported in [27]. Given that $1\text{Ha} = 27.2114\text{eV}$, we suspect there is a unit discrepancy in [28]. While the unit in their paper is listed as meV, we believe the correct unit should be mHa. Confirmed with the authors in the papers and we corrected it in our Table 7.*

Table 8 presents the results sampling as given in equation 6, as introduced in [27]. UniGenX achieves state-of-the-art (SOTA) performance on four out of six properties. Notably, for the property μ , our model demonstrates a significant improvement of 53.6% over the previous SOTA [46]. However, performance on α and C_v is slightly lower compared to [45]. This can be attributed to two factors: first, [45] employs separate models for each property, whereas UniGenX uses a unified model, potentially leading to performance trade-offs. Second, [45] incorporates post-generation molecular force field optimization, following [28], which leverages domain-specific expert knowledge. Our approach evaluates the model’s direct output without such optimization. While these differences may impact direct comparison, UniGenX still excels in key performance metrics, highlighting its versatility and robustness.

The properties in Table 8 were calculated for generated samples using an EGNN model, consistent with the EDM settings from [27]. The QM9 row indicates the EGNN model’s error estimation relative to the QM9 property labels. Notably, UniGenX’s generated results exhibit error closely approximating the validation model’s error. For instance, the MAE of HOMO energy level is identical to QM9 (39meV vs. 39meV), and the MAE of LUMO is lower (35meV vs. 36meV). This suggests that UniGenX’s performance may exceed the validation model’s capacity for accurate error assessment. A detailed discussion of this discrepancy is reserved for future work.

For the multiple-property generation task, we visualize the results in the following way: for a single property, we plot a kernel density histogram 10a; for two properties, we use a scatter plot 10b; and for three or more properties, we apply principal component analysis (PCA) to reduce the dimensions and plot a 2D scatter plot 11. These visualizations demonstrate that our model can flexibly generate molecules conditioned on varying numbers of properties, while maintaining stability and reliability.



(a) Kernel density estimate (KDE) plot comparing the distribution of the given target property and the predicted property values of generated molecules.

(b) Scatter plot showing the joint distribution of two predicted properties for generated molecules conditioned on given target properties.

Furthermore, four examples are displayed in Figure 12, in each example on the left is ground truth and on the right is the generated conformation.

4.3 Protein Results

As shown in Figure 13, for all proteins, our model successfully predicts native and unfolded states with similar topological features on the free energy landscape. The predicted two-dimensional free energy surfaces closely resemble those obtained from MD simulations. Notably, our model captures partial or complete folding intermediates that are visible on the landscape, demonstrating its capability to approximate the equilibrium distribution. Quantitatively, the average discrepancy between our model and molecular dynamics (MD) simulations on the 2D free energy landscapes is 0.91 kcal/mol, ranging from 0.64 kcal/mol for 1FME to 1.20 kcal/mol for A3D. Notably, this level of deviation is comparable to the expected differences between two classical MD force fields [47, 48], suggesting that UniGenX achieves near-physically consistent accuracy.

As shown in Table 9, UniGenX is able to generate protein sequences that not only match the target EC number but also exhibit strong structural quality and functional relevance. When comparing UniGenX with and without structural conditioning during training, we observe consistent improvements across both sequence-level and structure-level metrics. Specifically, models trained

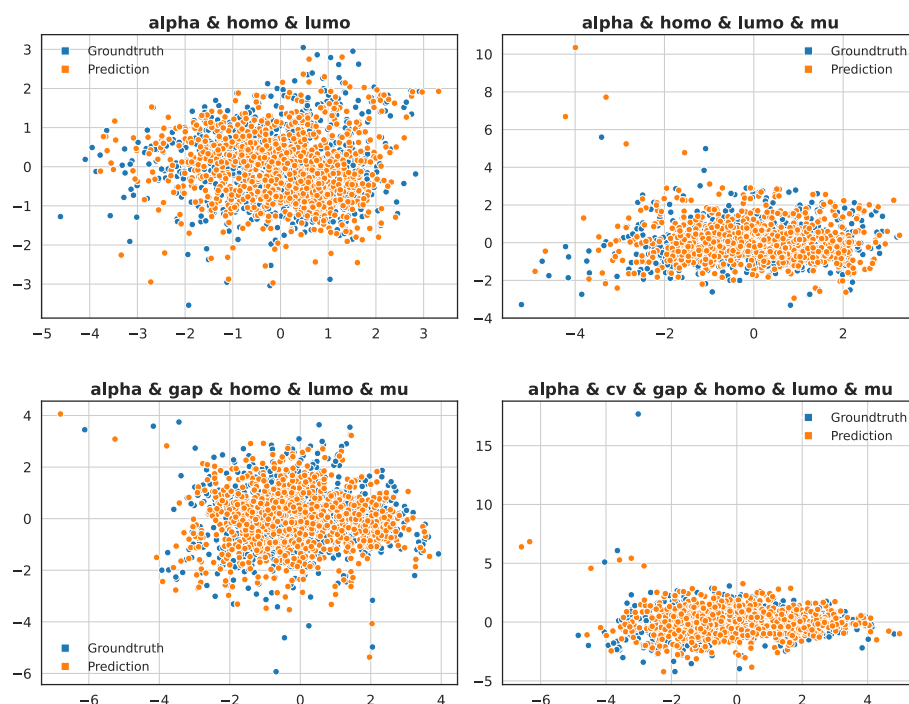


Figure 11: PCA projection of predicted properties of generated molecules conditioned on three or more target properties.

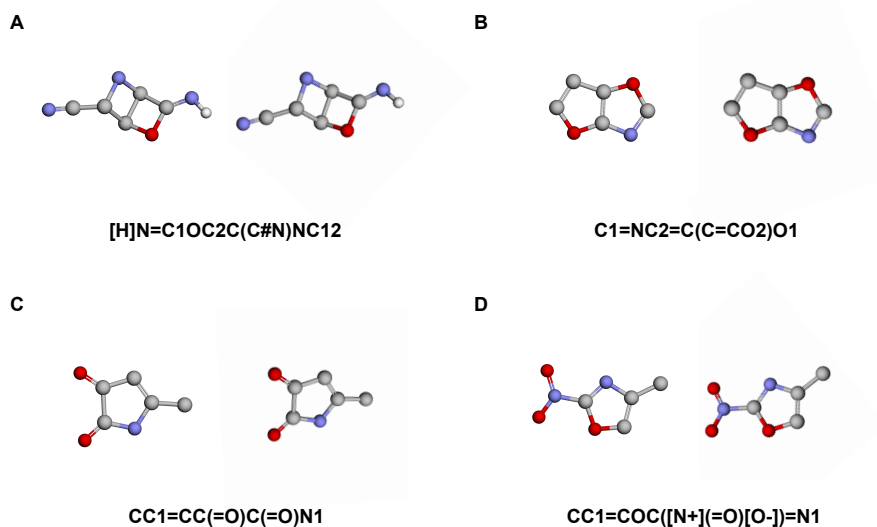


Figure 12: Examples of predicted structures. The groundtruth and predicted structures are shown side-by-side, with groundtruth on the left, generated structures on the right.

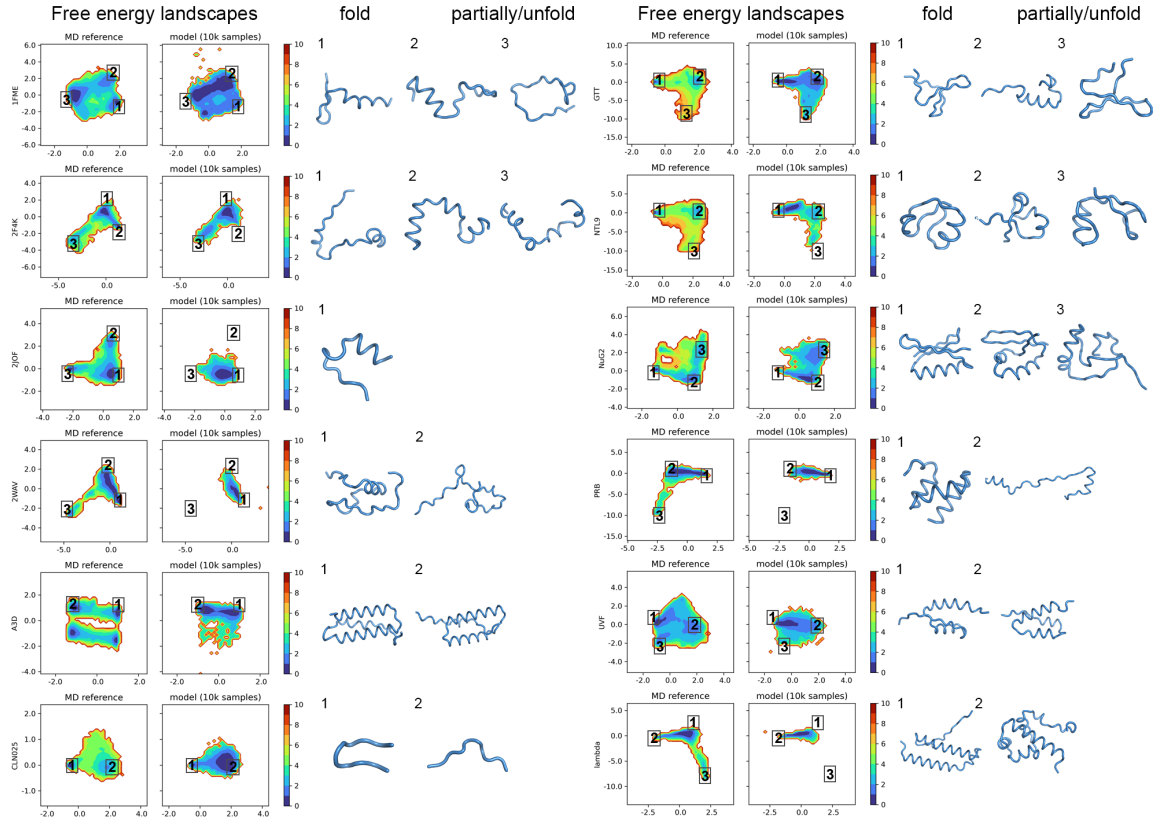


Figure 13: Free energy surfaces of DESRES fast-folding proteins. The landscapes on the left are obtained from long-timescale molecular dynamics (MD) simulations, while the landscapes on the right are generated by UniGenX. The model successfully captures the key features of the energy landscapes, including native and unfolded states, with an average deviation of only 0.91 kcal/mol from the MD reference—a discrepancy comparable to that between different classical force fields [47, 48]. Representative conformational states predicted by UniGenX are also shown.

with structural information yield higher pLDDT and pTM scores, along with significantly better TM-scores and lower RMSDs when benchmarked against both AFDB and PDB reference structures.

Moreover, comparison with structures predicted by ESMFold (Table 10) reveals a high degree of structural agreement: generated sequences consistently achieve TM-scores above 0.85 and low RMSD values, indicating that UniGenX reliably produces proteins that fold into plausible and stable 3D structures aligned with the intended enzymatic function.

Figure 14 presents one representative case for each of the three tested EC numbers. Notably, despite relatively low sequence identity to naturally occurring proteins, the generated sequences fold into structures with strong similarity to experimentally resolved counterparts. This demonstrates that UniGenX can generalize beyond sequence similarity, capturing structural patterns that are functionally meaningful and biophysically consistent.

Tested EC number		Overview			Sequence	
		pLDDT	pTM	Time(s)	Accuracy (%)	Avg. Top Hit Identity (%)
UniGenX	2.6.1.x	80.11	0.821	9.38	63.87	77.35
	3.1.1.x	87.25	0.883	3.77	76.42	75.31
	3.5.2.x	91.59	0.938	8.28	84.95	77.49
w/o struct.	2.6.1.x	74.96	0.766	9.20	69.48	71.58
	3.1.1.x	85.83	0.878	3.37	74.28	70.07
	3.5.2.x	87.46	0.911	9.13	79.91	71.84

Table 9: Evaluation of function-guided enzyme generation. The performance of UniGenX trained with both sequence and structure is compared to a sequence-only baseline. Including structural information during training leads to generated proteins with higher predicted structural quality (pLDDT, pTM) and functional accuracy.

Tested EC Number	RMSD (Å)	TM-score
2.6.1.x	4.398	0.916
3.1.1.x	6.047	0.867
3.5.2.x	3.206	0.936

Table 10: Structural comparison between UniGenX generated structures and ESMFold-predicted structures across three EC numbers.

4.4 Protein-Ligand Docking Results

We benchmark our proposed UniGenX (100M) model against a modified version of 3DMolformer[33], in which the diffusion module is replaced with a deterministic linear transformation. To ensure a fair comparison, both models adopt the same Transformer backbone and are trained under identical hyperparameters for 1,000 epochs using a cosine learning rate schedule. Quantitative results are presented in Table 11.

To complement these aggregate metrics with a more nuanced view of performance, Figure 15 shows the cumulative distribution functions (CDFs) of RMSD values for predicted ligand and pocket structures across different modeling setups. These curves reveal the proportion of samples below varying RMSD thresholds, offering a finer-grained perspective than summary statistics such as mean or median.

The first task evaluates the ability to predict ligand structures given both the apo and holo pocket conformations. UniGenX exhibits clear superiority across all metrics: the percentage of

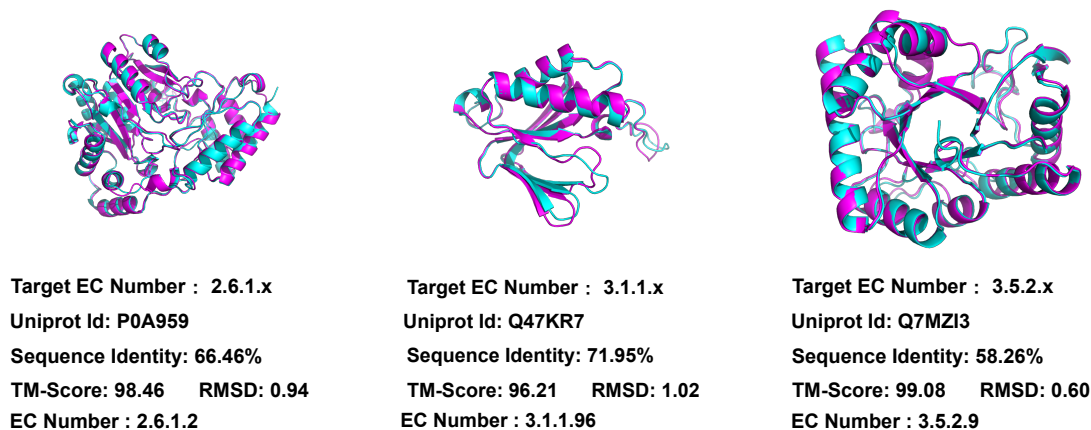
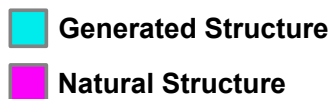


Figure 14: For all three cases, the proteins generated by UniGenX exhibit the close structural alignment to naturally occurring proteins with relative small sequence identity.

ligand predictions within 2\AA RMSD improves from 1.27% to 21.66%, representing a 17-fold increase, while the median RMSD drops from 3.82\AA to 2.37\AA . Consistent gains are also observed at the 25th and 75th percentiles, as well as in mean RMSD, indicating not only improved accuracy but also greater robustness across diverse samples.

The second task, which requires predicting both the holo pocket and ligand coordinates from the apo structure alone, presents a more demanding setting that involves modeling pocket rearrangements—an essential aspect of induced fit. Here, the advantages of UniGenX are even more pronounced. For pocket prediction, UniGenX achieves a median RMSD of 1.75\AA and a 2\AA success rate of 69.43%, compared to 2.96\AA and 12.10% for the baseline. For ligand prediction, the improvements are similarly substantial. When the pocket is provided (Pocket Gv), UniGenX reaches 24.84% within 2\AA RMSD, outperforming the baseline’s 18.47%. In the more challenging case where the pocket must also be inferred (Pocket Not Gv), UniGenX achieves 15.92% within 2\AA —an over 23-fold improvement compared to the baseline’s 0.64%.

Evaluation of the joint protein-ligand complex structure further underscores these gains: UniGenX reduces the mean RMSD from 4.20\AA to 2.72\AA . Taken together, these results demonstrate that UniGenX not only improves absolute prediction accuracy but also captures the coupled conformational dynamics of protein-ligand interactions. This ability to model joint structural distributions under dynamic settings is critical for advancing molecular design and docking beyond static approximations.

To further illustrate the qualitative fidelity of predicted structures, Figure 16 shows representative examples for two protein-ligand complexes (PDB IDs: 4KZQ and 2VVN) under both modeling conditions—with and without the holo pocket provided. In both cases, the predicted ligand structures (shown in cyan) exhibit strong agreement with the ground truth conformations, even when the pocket geometry must be inferred. These visual results reinforce the model’s ability to recover realis-

Table 11: Evaluation of UniGenX (100M) versus 3DMolFormer(100M) on dynamic pocket-ligand prediction. RMSD percentiles, mean values, and the percentage of predictions within 2Å and 5Å are reported for pocket, ligand, and complex structures.

Method	Percentiles ↓				% Below ↑	
	25%	50%	75%	Mean	2Å	5Å
<i>3DMolFormer (100M)</i> [33]						
Pocket + Ligand	3.03	3.82	4.66	4.20	1.27	82.17
Pocket	2.34	2.96	4.06	3.54	12.10	85.99
Ligand (Pocket Gv)	2.18	2.84	3.63	2.97	18.47	95.54
Ligand (Pocket Not Gv)	4.15	5.22	6.60	5.41	0.64	43.31
<i>UniGenX (100M)</i>						
Pocket + Ligand	2.05	2.37	2.94	2.72	21.66	95.54
Pocket	1.51	1.75	2.14	2.12	69.43	95.54
Ligand (Pocket Gv)	2.01	2.57	3.29	2.73	24.84	98.09
Ligand (Pocket Not Gv)	2.10	2.81	3.51	2.90	15.92	96.82

tic and physically plausible docking configurations, aligning well with the quantitative improvements described above.

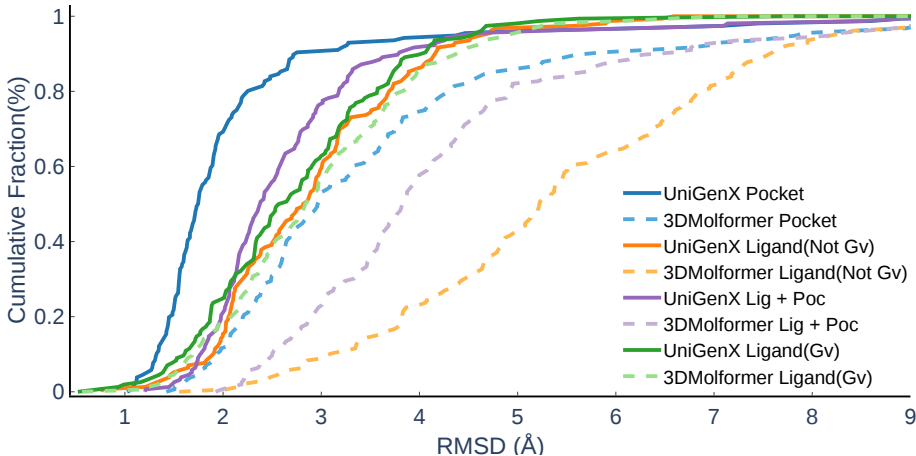


Figure 15: Cumulative Distribution of RMSD Values for Predicted Ligand and Pocket Structures.

4.5 Unification Results of molecule and materials

The finetuned results for MP-20, Carbon 24, MPTS-52 and GEOM-QM9 results can be found in Table 12 and Table 13. The results show that a 100M unification model UniGenX(100M) still performed better results than the SOTA methods on most indicators. With larger models and more data, our model can scale to achieve better results due to the scalability of the auto-aggressive and diffusion models. Additionally, due to the inclusion of a word loss head, our model is adaptable for language training, making it flexible for general tasks such as language-based design and generation.

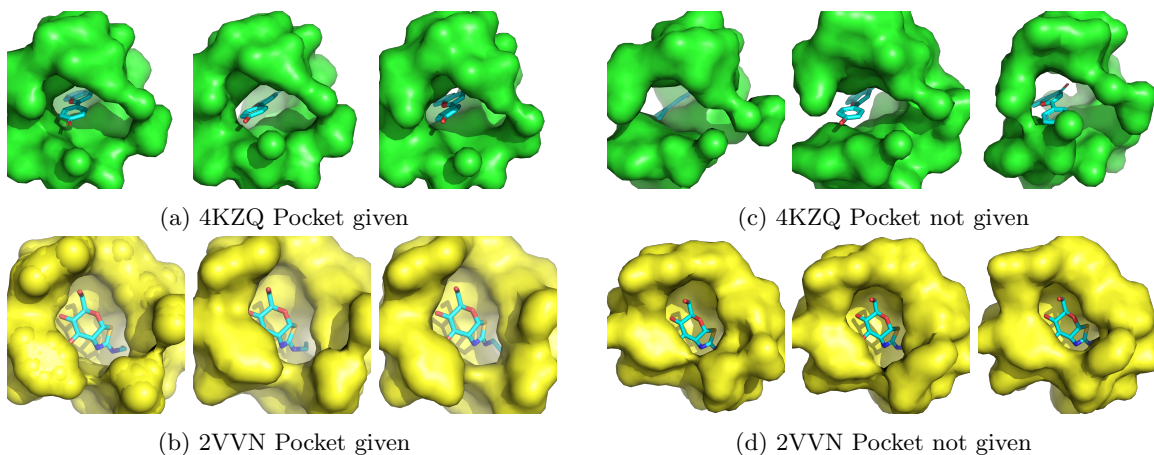


Figure 16: Examples of the docking predictions.

	MP-20		Carbon-24		MPTS-52	
Methods	MR(%) \uparrow	RMSD(\AA) \downarrow	MR(%) \uparrow	RMSD(\AA) \downarrow	MR(%) \uparrow	RMSD(\AA) \downarrow
CDVAE[15]	33.90	0.1045	17.09	0.2969	5.34	0.2106
DiffCSP[9]	51.49	0.063	17.54	0.2759	12.19	0.1786
FlowMM[10]	61.39	0.057	23.47	0.4122	17.54	0.1726
UniGenX(100M)	64.74	0.042	29.46	0.2318	32.97	0.0838

Table 12: Results of the unification model on material tasks. MR represents Match Rate. UniGenX’s performance surpasses the state-of-the-art, which proves its unified ability across diverse domains.

Dataset	Large-scale QM9							
Methods	COV-P (%) \uparrow		MAT-P (\AA) \downarrow		COV (%) \uparrow		MAT (\AA) \downarrow	
	Mean	Median	Mean	Median	Mean	Median	Mean	Median
ConfGF[24]	46.23	44.87	0.5171	0.5133	89.21	95.12	0.2809	0.2837
GeoMol[23]	78.28	81.03	0.3790	0.3861	91.05	95.55	0.2970	0.2993
DMCG[20]	90.86	95.36	0.2305	0.2258	98.34	100	0.1486	0.1340
UniGenX(100M)	91.43	100.00	0.2186	0.0818	92.53	100	0.1441	0.0818

Table 13: Results of the unification model on the small molecular task of GEOM-QM9 using COV-P, MAT-P, COV, and MAT metrics. COV-P, MAT-P, COV, and MAT evaluate molecule coverage and accuracy, as defined by Equations (1)–(4).

4.6 Intergrating with LLM Results

MP-20		
Methods	MR(%) \uparrow	RMSD(\AA) \downarrow
NatureLM[38]	61.78	0.044
UniGenX-NL(1B)	62.82	0.042

Table 14: Results of UniGenX with capability of natural language on MP-20.

As shown in Table 14, our model UniGenX-NL(1B), which incorporates natural language understanding capabilities, not only preserves but also improves upon the performance of prior models such as NatureLM. Specifically, it achieves a higher matching rate (MR) of 63.10% and a lower RMSD of 0.040 \AA , outperforming NatureLM on both metrics.

Table 15 show that comparing with UniGenX(100M), UniGenX-NL(1B) also performed better on QM9.

These results highlight the effectiveness of our approach in bridging linguistic understanding with structural prediction tasks. This also means that we can greatly enhance the model’s flexibility while maintaining its performance.

Dataset	Large-scale QM9							
Methods	COV-P (%) \uparrow		MAT-P (\AA) \downarrow		COV (%) \uparrow		MAT (\AA) \downarrow	
	Mean	Median	Mean	Median	Mean	Median	Mean	Median
UniGenX(100M)	91.43	100.00	0.2186	0.0818	92.53	100	0.1441	0.0818
UniGenX-NL(1B)	92.30	100.00	0.1518	0.0886	92.88	100	0.1368	0.0751

Table 15: Comparison between 100M model and Results of UniGenX with capability of natural language on QM9.

The results demonstrate that our model retains its linguistic capabilities without compromising accuracy. The synergistic effect of combining linguistic and numerical reasoning opens the door for developing unified models that can jointly process textual descriptions and scientific data. This paves the way for future applications such as text-guided molecule design, multimodal scientific assistants, and interactive generative systems in computational chemistry and materials science.

5 Conclusion

This work introduces UniGenX, a novel framework for unified generation of symbolic and numerical scientific data. UniGenX integrates an autoregressive model with a conditional diffusion-based generative head, leveraging the autoregressive model’s sequence flexibility and the diffusion model’s numerical precision. A key innovation is a sequentialization scheme that represents diverse scientific data—formulas, coordinates, energies, forces—as a single token sequence. This enables next-token prediction with the autoregressive component, while the diffusion head addresses numerical precision limitations by operating in continuous space and training efficiently on low-dimensional variables. UniGenX achieves significant performance improvements over state-of-the-art diffusion/flow matching models in material generation (10–120% gains on MP-20, Carbon-24, and MPTS-52), surpasses NatureLM, and establishes new state-of-the-art results on most targets in GEOM-QM9 prediction, de novo design on materials, and conditional generation on QM9. Demonstrating high capacity for unified training across domains and natural language prompt generation, UniGenX avoids explicit

inductive biases for equivariance/invariance, relying on data augmentation to learn these properties, thus preserving transformer scalability. Future work will extend UniGenX to other scientific data types—proteins, DNA—and tasks—energy/force prediction, aiming towards a unified foundation model for scientific generation, potentially integrating with general domain models.

References

- [1] Keith T Butler, Daniel W Davies, Hugh Cartwright, Olexandr Isayev, and Aron Walsh. Machine learning for molecular and materials science. *Nature*, 559(7715):547–555, 2018.
- [2] Jessica Vamathevan, Dominic Clark, Paul Czodrowski, Ian Dunham, Edgardo Ferran, George Lee, Bin Li, Anant Madabhushi, Parantu Shah, Michaela Spitzer, et al. Applications of machine learning in drug discovery and development. *Nature reviews Drug discovery*, 18(6):463–477, 2019.
- [3] Roald Hoffmann. How chemistry and physics meet in the solid state. *Angewandte Chemie International Edition in English*, 26(9):846–878, 1987.
- [4] Marcel L Verdonk, Jason C Cole, Michael J Hartshorn, Christopher W Murray, and Richard D Taylor. Improved protein–ligand docking using gold. *Proteins: Structure, Function, and Bioinformatics*, 52(4):609–623, 2003.
- [5] Carl Ivar Branden and John Tooze. *Introduction to protein structure*. Garland Science, 2012.
- [6] Josh Achiam, Steven Adler, Sandhini Agarwal, Lama Ahmad, Ilge Akkaya, Florencia Leoni Aleman, Diogo Almeida, Janko Altschmidt, Sam Altman, Shyamal Anadkat, et al. Gpt-4 technical report. *arXiv preprint arXiv:2303.08774*, 2023.
- [7] Hugo Touvron, Thibaut Lavril, Gautier Izacard, Xavier Martinet, Marie-Anne Lachaux, Timothée Lacroix, Baptiste Rozière, Naman Goyal, Eric Hambro, Faisal Azhar, et al. Llama: Open and efficient foundation language models. *arXiv preprint arXiv:2302.13971*, 2023.
- [8] Jonathan Ho, Ajay Jain, and Pieter Abbeel. Denoising diffusion probabilistic models. *Advances in neural information processing systems*, 33:6840–6851, 2020.
- [9] Rui Jiao, Wenbing Huang, Peijia Lin, Jiaqi Han, Pin Chen, Yutong Lu, and Yang Liu. Crystal structure prediction by joint equivariant diffusion. *Advances in Neural Information Processing Systems*, 36:17464–17497, 2023.
- [10] Benjamin Kurt Miller, Ricky TQ Chen, Anuroop Sriram, and Brandon M Wood. Flowmm: Generating materials with riemannian flow matching. *arXiv preprint arXiv:2406.04713*, 2024.
- [11] Andrey A Toropov, Alla P Toropova, Dilya V Mukhamedzhanova, and Ivan Gutman. Simplified molecular input line entry system (smiles) as an alternative for constructing quantitative structure-property relationships (qspr). *Indian Journal of Chemistry-Section A Inorganic, Physical, Theoretical and Analytical Chemistry*, 44(8):1545–1552, 2005.
- [12] Giuseppe Grosso and Giuseppe Pastori Parravicini. *Solid state physics*. Academic press, 2013.
- [13] Anubhav Jain, Shyue Ping Ong, Geoffroy Hautier, Wei Chen, William Davidson Richards, Stephen Dacek, Shreyas Cholia, Dan Gunter, David Skinner, Gerbrand Ceder, and Kristin a. Persson. The Materials Project: A materials genome approach to accelerating materials innovation. *APL Materials*, 1(1):011002, 2013.
- [14] Chris J. Pickard. Airss data for carbon at 10gpa and the c+n+h+o system at 1gpa, 2020.
- [15] Tian Xie, Xiang Fu, Octavian-Eugen Ganea, Regina Barzilay, and Tommi Jaakkola. Crystal diffusion variational autoencoder for periodic material generation. *arXiv preprint arXiv:2110.06197*, 2021.

- [16] Shyue Ping Ong, William Davidson Richards, Anubhav Jain, Geoffroy Hautier, Michael Kocher, Shreyas Cholia, Dan Gunter, Vincent L Chevrier, Kristin A Persson, and Gerbrand Ceder. Python materials genomics (pymatgen): A robust, open-source python library for materials analysis. *Computational Materials Science*, 68:314–319, 2013.
- [17] Claudio Zeni, Robert Pinsler, Daniel Zügner, Andrew Fowler, Matthew Horton, Xiang Fu, Zilong Wang, Aliaksandra Shysheya, Jonathan Crabbé, Shoko Ueda, et al. A generative model for inorganic materials design. *Nature*, pages 1–3, 2025.
- [18] Tero Karras, Miika Aittala, Tuomas Kynkäänniemi, Jaakko Lehtinen, Timo Aila, and Samuli Laine. Guiding a diffusion model with a bad version of itself. *arXiv preprint arXiv:2406.02507*, 2024.
- [19] Han Yang, Chenxi Hu, Yichi Zhou, Xixian Liu, Yu Shi, Jieliang Li, Guanzhi Li, Zekun Chen, Shuizhou Chen, Claudio Zeni, et al. Mattersim: A deep learning atomistic model across elements, temperatures and pressures. *arXiv preprint arXiv:2405.04967*, 2024.
- [20] Jinhua Zhu, Yingce Xia, Chang Liu, Lijun Wu, Shufang Xie, Yusong Wang, Tong Wang, Tao Qin, Wengang Zhou, Houqiang Li, et al. Direct molecular conformation generation. *arXiv preprint arXiv:2202.01356*, 2022.
- [21] Simon Axelrod and Rafael Gomez-Bombarelli. Geom, energy-annotated molecular conformations for property prediction and molecular generation. *Scientific Data*, 9(1):185, 2022.
- [22] Raghunathan Ramakrishnan, Pavlo O Dral, Matthias Rupp, and O Anatole von Lilienfeld. Quantum chemistry structures and properties of 134 kilo molecules. *Scientific Data*, 1, 2014.
- [23] Octavian Ganea, Lagnajit Pattanaik, Connor Coley, Regina Barzilay, Klavs Jensen, William Green, and Tommi Jaakkola. Geomol: Torsional geometric generation of molecular 3d conformer ensembles. *Advances in Neural Information Processing Systems*, 34:13757–13769, 2021.
- [24] Chence Shi, Shitong Luo, Minkai Xu, and Jian Tang. Learning gradient fields for molecular conformation generation. In *International conference on machine learning*, pages 9558–9568. PMLR, 2021.
- [25] Congsheng Xu, Yi Lu, Xiaomei Deng, and Peiyuan Yu. Prediction of molecular conformation using deep generative neural networks. *Chinese Journal of Chemistry*, 41(24):3684–3688, 2023.
- [26] Daniel GA Smith, Lori A Burns, Andrew C Simmonett, Robert M Parrish, Matthew C Schieber, Raimondas Galvelis, Peter Kraus, Holger Kruse, Roberto Di Remigio, Asem Alenaizan, et al. Psi4 1.4: Open-source software for high-throughput quantum chemistry. *The Journal of chemical physics*, 152(18), 2020.
- [27] Emiel Hoogeboom, Victor Garcia Satorras, Clément Vignac, and Max Welling. Equivariant diffusion for molecule generation in 3d. In *International conference on machine learning*, pages 8867–8887. PMLR, 2022.
- [28] Yuning You, Ruida Zhou, Jiwoong Park, Haotian Xu, Chao Tian, Zhangyang Wang, and Yang Shen. Latent 3d graph diffusion. In *International Conference on Learning Representations*, 2024.
- [29] Kresten Lindorff-Larsen, Stefano Piana, Ron O Dror, and David E Shaw. How fast-folding proteins fold. *Science*, 334(6055):517–520, 2011.

- [30] Tianhao Yu, Haiyang Cui, Jianan Canal Li, Yunan Luo, Guangde Jiang, and Huimin Zhao. Enzyme function prediction using contrastive learning. *Science*, 379(6639):1358–1363, 2023.
- [31] Zeming Lin, Halil Akin, Roshan Rao, Brian Hie, Zhongkai Zhu, Wenting Lu, Nikita Smetanin, Robert Verkuil, Ori Kabeli, Yaniv Shmueli, et al. Evolutionary-scale prediction of atomic-level protein structure with a language model. *Science*, 379(6637):1123–1130, 2023.
- [32] Michel van Kempen, Stephanie S Kim, Charlotte Tumescheit, Milot Mirdita, Cameron LM Gilchrist, Johannes Söding, and Martin Steinegger. Foldseek: fast and accurate protein structure search. *Biorxiv*, pages 2022–02, 2022.
- [33] Xiuyuan Hu, Guoqing Liu, Can Chen, Yang Zhao, Hao Zhang, and Xue Liu. 3dmolformer: A dual-channel framework for structure-based drug discovery. *arXiv preprint arXiv:2502.05107*, 2025.
- [34] Till Siebenmorgen, Filipe Menezes, Sabrina Benassou, Erinc Merdivan, Kieran Didi, André Santos Dias Mourão, Radosław Kitel, Pietro Liò, Stefan Kesselheim, Marie Piraud, et al. Misato: machine learning dataset of protein–ligand complexes for structure-based drug discovery. *Nature computational science*, 4(5):367–378, 2024.
- [35] John Jumper, Richard Evans, Alexander Pritzel, Tim Green, Michael Figurnov, Olaf Ronneberger, Kathryn Tunyasuvunakool, Russ Bates, Augustin Žídek, Anna Potapenko, et al. Highly accurate protein structure prediction with alphafold. *nature*, 596(7873):583–589, 2021.
- [36] Zhihai Liu, Yan Li, Li Han, Jie Li, Jie Liu, Zhixiong Zhao, Wei Nie, Yuchen Liu, and Renxiao Wang. Pdb-wide collection of binding data: current status of the pdbbind database. *Bioinformatics*, 31(3):405–412, 2015.
- [37] Minyi Su, Qifan Yang, Yu Du, Guoqin Feng, Zhihai Liu, Yan Li, and Renxiao Wang. Comparative assessment of scoring functions: the casf-2016 update. *Journal of chemical information and modeling*, 59(2):895–913, 2018.
- [38] Yingce Xia, Peiran Jin, Shufang Xie, Liang He, Chuan Cao, Renqian Luo, Guoqing Liu, Yue Wang, Zequn Liu, Yuan-Jyue Chen, et al. Naturelm: Deciphering the language of nature for scientific discovery. *arXiv preprint arXiv:2502.07527*, 2025.
- [39] Clement Vignac, Igor Krawczuk, Antoine Siraudin, Bohan Wang, Volkan Cevher, and Pascal Frossard. Digress: Discrete denoising diffusion for graph generation. *arXiv preprint arXiv:2209.14734*, 2022.
- [40] Xinyi Zhou, Xing Li, Yingzhao Lian, Yiwen Wang, Lei Chen, Mingxuan Yuan, Jianye Hao, Guangyong Chen, and Pheng Ann Heng. Seadag: Semi-autoregressive diffusion for conditional directed acyclic graph generation, 2024.
- [41] Victor Garcia Satorras, Emiel Hoogeboom, Fabian Fuchs, Ingmar Posner, and Max Welling. E(n) equivariant normalizing flows. *Advances in Neural Information Processing Systems*, 34:4181–4192, 2021.
- [42] Minkai Xu, Alexander S Powers, Ron O Dror, Stefano Ermon, and Jure Leskovec. Geometric latent diffusion models for 3d molecule generation. In *International Conference on Machine Learning*, pages 38592–38610. PMLR, 2023.

- [43] Yuxuan Song, Jingjing Gong, Yanru Qu, Hao Zhou, Mingyue Zheng, Jingjing Liu, and Wei-Ying Ma. Unified generative modeling of 3d molecules via bayesian flow networks. *arXiv preprint arXiv:2403.15441*, 2024.
- [44] Xiner Li, Limei Wang, Youzhi Luo, Carl Edwards, Shurui Gui, Yuchao Lin, Heng Ji, and Shuiwang Ji. Geometry informed tokenization of molecules for language model generation. *arXiv preprint arXiv:2408.10120*, 2024.
- [45] Kaiyuan Gao, Yusong Wang, Haoxiang Guan, Zun Wang, Qizhi Pei, John E. Hopcroft, Kun He, and Lijun Wu. Tokenizing 3d molecule structure with quantized spherical coordinates, 2024.
- [46] Xiner Li, Limei Wang, Youzhi Luo, Carl Edwards, Shurui Gui, Yuchao Lin, Heng Ji, and Shuiwang Ji. Geometry informed tokenization of molecules for language model generation, 2024.
- [47] Robert B Best and Jeetain Mittal. Free-energy landscape of the gbl hairpin in all-atom explicit solvent simulations with different force fields: Similarities and differences. *Proteins: Structure, Function, and Bioinformatics*, 79(4):1318–1328, 2011.
- [48] David F Hahn, Vytutas Gapsys, Bert L de Groot, David L Mobley, and Gary Tresadern. Current state of open source force fields in protein–ligand binding affinity predictions. *Journal of Chemical Information and Modeling*, 64(13):5063–5076, 2024.
- [49] Hugo Touvron, Louis Martin, Kevin Stone, Peter Albert, Amjad Almahairi, Yasmine Babaei, Nikolay Bashlykov, Soumya Batra, Prajjwal Bhargava, Shruti Bhosale, et al. Llama 2: Open foundation and fine-tuned chat models. *arXiv preprint arXiv:2307.09288*, 2023.
- [50] Aaron Grattafiori, Abhimanyu Dubey, Abhinav Jauhri, Abhinav Pandey, Abhishek Kadian, Ahmad Al-Dahle, Aiesha Letman, Akhil Mathur, Alan Schelten, Alex Vaughan, et al. The llama 3 herd of models. *arXiv preprint arXiv:2407.21783*, 2024.
- [51] A Vaswani. Attention is all you need. *Advances in Neural Information Processing Systems*, 2017.
- [52] Jiaming Song, Chenlin Meng, and Stefano Ermon. Denoising diffusion implicit models. In *International Conference on Learning Representations*, 2020.
- [53] Yang Song, Jascha Sohl-Dickstein, Diederik P Kingma, Abhishek Kumar, Stefano Ermon, and Ben Poole. Score-based generative modeling through stochastic differential equations. *arXiv preprint arXiv:2011.13456*, 2020.
- [54] Tero Karras, Miika Aittala, Timo Aila, and Samuli Laine. Elucidating the design space of diffusion-based generative models. *Advances in neural information processing systems*, 35:26565–26577, 2022.
- [55] Diederik Kingma, Tim Salimans, Ben Poole, and Jonathan Ho. Variational diffusion models. *Advances in neural information processing systems*, 34:21696–21707, 2021.
- [56] Yang Song and Stefano Ermon. Generative modeling by estimating gradients of the data distribution. *Advances in neural information processing systems*, 32, 2019.
- [57] Lawrence C Evans. *An introduction to stochastic differential equations*, volume 82. American Mathematical Soc., 2012.

- [58] Yaron Lipman, Ricky TQ Chen, Heli Ben-Hamu, Maximilian Nickel, and Matt Le. Flow matching for generative modeling. *arXiv preprint arXiv:2210.02747*, 2022.
- [59] Yaron Lipman, Marton Havasi, Peter Holderrieth, Neta Shaul, Matt Le, Brian Karrer, Ricky TQ Chen, David Lopez-Paz, Heli Ben-Hamu, and Itai Gat. Flow matching guide and code. *arXiv preprint arXiv:2412.06264*, 2024.
- [60] Xingchao Liu, Chengyue Gong, and Qiang Liu. Flow straight and fast: Learning to generate and transfer data with rectified flow. *arXiv preprint arXiv:2209.03003*, 2022.
- [61] Nanye Ma, Mark Goldstein, Michael S Albergo, Nicholas M Boffi, Eric Vanden-Eijnden, and Saining Xie. Sit: Exploring flow and diffusion-based generative models with scalable interpolant transformers. In *European Conference on Computer Vision*, pages 23–40. Springer, 2024.
- [62] Michael S Albergo, Nicholas M Boffi, and Eric Vanden-Eijnden. Stochastic interpolants: A unifying framework for flows and diffusions. *arXiv preprint arXiv:2303.08797*, 2023.
- [63] Anubhav Jain, Shyue Ping Ong, Geoffroy Hautier, Wei Chen, William Davidson Richards, Stephen Dacek, Shreyas Cholia, Dan Gunter, David Skinner, Gerbrand Ceder, et al. Commentary: The materials project: A materials genome approach to accelerating materials innovation. *APL materials*, 1(1), 2013.
- [64] Markus Scheidgen, Lauri Himanen, Alvin Noe Ladines, David Sikter, Mohammad Nakhaee, Adam Fekete, Theodore Chang, Amir Golparvar, José A. Márquez, Sandor Brockhauser, Sebastian Brückner, Luca M. Ghiringhelli, Felix Dietrich, Daniel Lehmberg, Thea Denell, Andrea Albino, Hampus Näsström, Sherjeel Shabih, Florian Dobener, Markus Kühbach, Rubel Mozumder, Joseph F. Rudzinski, Nathan Daelman, José M. Pizarro, Martin Kuban, Cuauhtemoc Salazar, Pavel Ondračka, Hans-Joachim Bungartz, and Claudia Draxl. Nomad: A distributed web-based platform for managing materials science research data. *Journal of Open Source Software*, 8(90):5388, 2023.
- [65] James E. Saal, Scott Kirklin, Muratahan Aykol, Bryce Meredig, and C. Wolverton. Materials design and discovery with high-throughput density functional theory: The open quantum materials database (oqmd). *JOM*, 65(11):1501–1509, 2013.
- [66] Scott Kirklin, James E. Saal, Bryce Meredig, Alex Thompson, Jeff W. Doak, Muratahan Aykol, Stephan Rühl, and Chris Wolverton. The open quantum materials database (oqmd): assessing the accuracy of dft formation energies. *npj Computational Materials*, 1(1):15010, 2015.
- [67] Chris J Pickard. Airss data for carbon at 10gpa and the c+ n+ h+ o system at 1gpa. (*No Title*), 2020.

A Auto-regressive model, diffusion model and flow matching

A.1 Autoregressive Model

Auto-regressive models have become a cornerstone in deep learning for sequential data modeling. These models operate by factorizing the joint probability distribution of a sequence into a product of conditional probabilities, allowing each token or data point to be predicted based on the preceding ones. Formally, given a sequence

$$\mathbf{x} = x_1, x_2, \dots, x_T,$$

the auto-regressive approach models the probability as

$$P(\mathbf{x}) = \prod_{t=1}^T P(x_t \mid x_1, x_2, \dots, x_{t-1}),$$

where x_i is the i -th token or element in the sequence. This property makes them highly effective for tasks such as language modeling, where predicting the next word in a sentence requires contextual understanding of the preceding words. Popular examples include models like the GPT series [6] and LLaMA [7, 49, 50], which primarily utilize multi-head attention-based Transformer [51] decoder architectures to capture long-range dependencies in data.

A.2 Diffusion Models

A.2.1 Diffusion Process

A diffusion model is defined by a diffusion process $\{x_t\}_{t=0}^1$, starts with $x \sim p_0$, and evolves to $x_1 \sim p_1$, where p_1 has a tractable form for efficient sample generation. The dataset of independent samples from the data distribution is available. Let $p(x_t)$ denote the probability density of x_t , and $p(x_t \mid x)$ represent the transition kernel from x to x_t , with $0 < t \leq 1$. The diffusion process is modeled as the solution to a stochastic differential equation (SDE) [52]:

$$dx_t = f(x_t, t)dt + g(t)d\mathbf{B}_t, \quad (7)$$

where \mathbf{B}_t is a standard Wiener process, $f(\cdot, t) : \mathbb{R}^d \rightarrow \mathbb{R}^d$ is the drift coefficient of $x(t)$, and $g(\cdot) : \mathbb{R} \rightarrow \mathbb{R}$ is the diffusion coefficient of $x(t)$.

By reversing the diffusion process, starting from samples $x_1 \sim p_1$, where p_1 is usually a Gaussian distribution, it is possible to recover samples $x \sim p_0$. The reverse of a diffusion process is also a diffusion process, governed by the reverse-time SDE [53]:

$$dx_t = [f(x_t, t) - g(t)^2 \nabla_{x_t} \log p_t(x_t)] dt + g(t)d\overline{\mathbf{B}}, \quad (8)$$

where $\overline{\mathbf{B}}$ is another standard Wiener process, i.e., Brownian motion from $t = 1$ to $t = 0$.

As the diffusion process is a stochastic process with the Brownian motion stochastic term, the SDE (7) of the forward process implies the following relationship

$$p(x_t) = \int_x p(x_t \mid x)p(x)dx, \quad (9)$$

where the conditional probability $p(x_t \mid x) = C \exp(-\frac{\|x_t - \alpha_t x\|^2}{\sigma_t^2})$, and C is the normalization constant satisfying $\int_{x_t} C \exp(-\frac{\|x_t - \alpha_t x\|^2}{\sigma_t^2}) dx_t = 1$. Equivalently, we have

$$x_t = \alpha_t x + \sigma_t \epsilon. \quad (10)$$

Here α_t and σ_t are linear and variance variable, depending on the time t ; ϵ is a random variable. In the diffusion model, α_t and σ_t are given by designed schemes for VE and VP cases [53]; the random variable ϵ is a standard Gaussian noise variable, i.e., $\epsilon \sim N(0, I)$. In our work, we use the Denoising Diffusion Probabilistic Model (DDPM) setting for training and the VP scheme for sampling [8, 52]. We also test the diffusion choice of Elucidated Diffusion Model (EDM) [54]. We obtained similar performance leveraging DDPM and EDM respectively, and listed the results as an ablation study in Appendix E.3.2.

A.2.2 Diffusion Targets

Different from conventional supervised learning, the training targets in the training loss of the diffusion model are not obvious most of the time. With the same noising process, the training targets differ between different models, such as ϵ model [8], denoising model [55], and score model [56].

Here we would show that all of these targets have connected forms. Recall that adding noise by $x_t = \alpha_t x + \sigma_t \epsilon$, i.e.,

$$p(x_t|x) = C e^{-\frac{\|x_t - \alpha_t x\|^2}{2\sigma_t^2}}. \quad (11)$$

By the definition of the score function $s(x_t) \equiv \nabla_{x_t} \log p(x_t)$ and through a direct calculation, we have

$$s(x_t) = \frac{\int_x \frac{\nabla_{x_t} p(x_t|x)}{p(x_t|x)} p(x_t|x) p(x) dx}{p(x_t)} = \int_x \nabla_{x_t} \log p(x_t|x) p(x|x_t) dx, \quad (12)$$

where we finally obtain

$$s(x_t) = \mathbb{E}_x[\nabla_{x_t} \log p(x_t|x)|x_t] = \mathbb{E}_x[-\frac{x_t - \alpha_t x}{\sigma_t^2}|x_t] = -\frac{x_t - \alpha_t \mathbb{E}[x|x_t]}{\sigma_t^2}. \quad (13)$$

By Theorem 1, the score of a distribution, $\nabla_{x_t} \log p_t(x_t)$, can be estimated by training a score-based model s_θ using score matching [56] with the training target $\nabla_{x_t} \log p(x_t|x)$. To approximate $\nabla_{x_t} \log p(x_t)$, a time-dependent score-based model $s_\theta(x_t, t)$ can be trained using a continuous generalization of the score matching objective [53]:

$$\theta^* = \arg \min_{\theta} \mathbb{E}_{t \sim U[0,1]} \left\{ \lambda(t) \mathbb{E}_x \mathbb{E}_{x_t|x} [\|s_\theta(x_t, t) - \nabla_{x_t} \log p(x_t|x)\|_2^2] \right\},$$

where $\lambda : [0, 1] \rightarrow \mathbb{R}^+$ is a weighting function, $U[0, 1]$ is a uniform distribution in $[0, 1]$, $x \sim p_0$ and p_0 is the data distribution.

From Eq. (13), one can also approximate the training target with a different model, such as the denoising model s_θ with the target x [55], and the ϵ model ϵ_θ [8] with the target $\frac{x_t - \alpha_t x}{\sigma_t} = \epsilon$, with a similar training loss as the score model. Hence, the optimal solution of the models (denoted as θ^*) approaches:

$$s_{\theta^*} \rightarrow \mathbb{E}_x[\nabla_{x_t} \log p(x_t|x)|x_t]; \quad \epsilon_{\theta^*} \rightarrow \mathbb{E}_x[\frac{x_t - \alpha_t x}{\sigma_t}|x_t]; \quad x_{\theta^*} \rightarrow \mathbb{E}_x[x|x_t]. \quad (14)$$

These models connect to each other in the optimal results given by Eq. (13), and have the following forms

$$\begin{aligned} s_{\theta^*}(x_t) &= -\frac{x_t - \alpha_t x_{\theta^*}(x_t)}{\sigma_t^2} \\ s_{\theta^*}(x_t) &= -\frac{\epsilon_{\theta^*}(x_t)}{\sigma_t}. \end{aligned} \quad (15)$$

Therefore, when training diffusion models using an ϵ model or denoising model, the sampling process can be aligned with score-based models via Eq. (15) and utilize the reverse stochastic differential equation (8). In this work, we adopt the ϵ model proposed in DDPM [8] for training and employ the VP scheme [53] for sampling.

A.3 Connections of the Training Targets

When the random variable z is a standard Gaussian random variable, i.e., $z = \epsilon$, we can express the connection between the diffusion model training targets and the training target v in flow matching. From the property of conditional expectation, $x_t = \mathbb{E}[x_t|x_t]$, one can obtain

$$x_t = \mathbb{E}[x_t|x_t] = \mathbb{E}[\alpha_t x + \sigma_t \epsilon|x_t] = \alpha_t \mathbb{E}[x|x_t] + \sigma_t \mathbb{E}[\epsilon|x_t]. \quad (16)$$

From diffusion models, $x_{\theta^*} = \mathbb{E}[x|x_t]$ gives the training target of the denoising model, and $\epsilon_{\theta^*} = \mathbb{E}[\epsilon|x_t]$ gives the training target of the ϵ model. From Eq. (13), we have

$$s(x_t) = -\frac{x_t - \alpha_t \mathbb{E}[x|x_t]}{\sigma_t^2}. \quad (17)$$

A direct calculation according to Eq. (21), (16), and (17) yields the connections of the diffusion targets s_{θ^*} , $\epsilon_{\theta^*} = \mathbb{E}[\epsilon|x_t]$, and $x_{\theta^*} = \mathbb{E}[x|x_t]$ with the flow matching target v as

$$\begin{aligned} s_{\theta^*} &= \frac{\alpha_t v - \dot{\alpha}_t x_t}{\dot{\alpha}_t \sigma_t - \alpha_t \dot{\sigma}_t} \sigma_t^{-1}; \\ \epsilon_{\theta^*} &= \frac{\dot{\alpha}_t x_t - \alpha_t v}{\dot{\alpha}_t \sigma_t - \alpha_t \dot{\sigma}_t}; \\ x_{\theta^*} &= \frac{\dot{\sigma}_t x_t - \sigma_t v}{\dot{\sigma}_t \alpha_t - \sigma_t \dot{\alpha}_t}. \end{aligned} \quad (18)$$

A.4 Diffusion model and flow matching

The training targets for diffusion and flow matching models share the same mathematical structure, as stated by Theorem 1 [57].

Theorem 1. *Let X be an integrable random variable. Then, for each σ -algebra \mathcal{V} and $Y \in \mathcal{V}$, $Z = \mathbb{E}(X|\mathcal{V})$ solves the least squares problem*

$$\min_{Z_{\theta} \in \mathcal{V}} \|Z_{\theta} - X\|,$$

where $\|X\| = \left(\int X^2 dP\right)^{\frac{1}{2}}$.

Diffusion models and flow matching share the same noising procedure, given by Eq. (10), i.e.,

$$x_t = \alpha_t x + \sigma_t z, \quad (19)$$

where $x \sim p_0$, p_0 is the data distribution, $z \sim p_{\text{prior}}$, p_{prior} is a prior distribution from which samples can be easily drawn. In diffusion models, the prior random variable is a standard Gaussian distribution, i.e., $z = \epsilon \sim N(0, I)$, thus limiting the diffusion process to approach Gaussian noise from the data variable. However, flow matching extends the prior to any distribution, making it a flow from samples of the given distribution to the generated data samples [58, 59]. Rectified flow

and stochastic interpolation can also be obtained through similar approaches [60, 61, 62]. A typical training target is to find the velocity that connects the prior and data distributions, $\frac{dx_t}{dt} = v$. Hence, the training target is directly derived from Eq. (10) as

$$\frac{dx_t}{dt} = \dot{\alpha}_t x + \dot{\sigma}_t z, \quad (20)$$

with the neural network $v_\theta(x_t)$ approximating the velocity v of the flow by

$$v = \mathbb{E} \left[\frac{dx_t}{dt} \middle| x_t \right] = \mathbb{E} [\dot{\alpha}_t x + \dot{\sigma}_t z | x_t] = \dot{\alpha}_t \mathbb{E} [x | x_t] + \dot{\sigma}_t \mathbb{E} [z | x_t]. \quad (21)$$

The score target, denoising model target, and ϵ target for flow matching with the Gaussian noise can also be derived from Eq. (13) and direct calculation, as discussed in Appendix A.3. In this work, we primarily focus on the combination of autoregressive models and diffusion models, as the combination with flow matching is similar to that with diffusion models. Therefore, this investigation is left for future discussion.

B Pseudocode

We provide the overall algorithm pseudocode, which includes the forward and sample processes for the model, as well as the forward and sample processes for diffloss. The algorithms are listed as follows.

Algorithm 1 UniGenX Forward Procedure

Require:

- w_{gt} : Ids of input tokens in the input sentences
 - v_{gt} : Numeral values in the input sentences
 - m_{val} : Masks for values
 - m_{pad} : Padding Masks
 - n : Multiplication times of DiffLoss
 - w : Loss weight
- 1: Initialize x_{input} in the shape of w_{gt}
 - 2: **# Embed the inputs**
 - 3: $x_{input}[\neg m_v] \leftarrow \text{Embedding}(w)$
 - 4: $x_{input}[m_v] \leftarrow \text{Linear}(v)$
 - 5: **# Pass through the AR Model**
 - 6: $h_{rep} \leftarrow \text{Transformer_Decoder}(x_{input}, m_{pad})$
 - 7: $w_{logits} \leftarrow \text{Linear}(h_{rep}[\neg m_{val}])$
 - 8: **# Compute the diffloss and wordloss**
 - 9: $l_d \leftarrow \text{DiffLoss}(v_{gt}, h_{rep}[:, -1][m_{val}], n)$
 - 10: $l_w \leftarrow \text{CrossEntropyLoss}(w_{gt}, w_{logits}[:, -1])$
 - 11: **return** $l_d + w * l_w$
-

Algorithm 2 DiffLoss Forward Procedure

Require:

v_{gt} : Ground truth numeral values
 h_{rep} : Hidden representations for conditional diffusion
 M : Times of Multiplication of DiffLoss

- 1: Initialize $\text{net} \leftarrow \text{SimpleMLPAdaLN}()$, $\text{diff} \leftarrow \text{GaussianDiffusion}()$
- 2: **# Apply DiffMul**
- 3: $v \leftarrow v_{gt}.\text{repeat}(M)$
- 4: $h \leftarrow h_{rep}.\text{repeat}(M)$
- 5: **# Sample Different Timesteps for Diff**
- 6: $T \leftarrow \text{diff.num_timesteps}$
- 7: $t \leftarrow \text{Randint}(0, T, (h_{rep}.\text{shape}[0],))$
- 8: **# Apply Diffusion**
- 9: $l \leftarrow \text{diff.trainingloss}(\text{net}, v_{gt}, t, h_{rep})$
- 10: **return** l

Algorithm 3 GaussianDiffusion Training Loss

Require:

net : Neural network for predicting noise and variance
 x_0 : Hidden representations for conditional diffusion
 t : Timesteps for Diffusion
 c : Condition for Diffusion

- 1: Sample ϵ from $\mathcal{N}(\mathbf{0}, \mathbf{I})$
- 2: $x_t \leftarrow \sqrt{\alpha_t}x_0 + \sqrt{1 - \alpha_t}\epsilon$
- 3: **# Predict Noise and Variance using**
- 4: $\hat{\epsilon}, \hat{\sigma} = \text{net}(x_t, t, c).\text{split}()$
- 5: **# Compute L2 loss and VLB loss**
- 6: $L_{mse} \leftarrow \text{L2Loss}(\hat{\epsilon}, \epsilon)$
- 7: $L_{vlb} \leftarrow \text{VLBloss}(\hat{\epsilon}.\text{detach}(), \hat{\sigma}, x_t, t)$
- 8: **return** $\text{mean_flat}(L_2 + L_{vlb})$

Algorithm 4 UniGenX Sampling Procedure

Require:

w_{in} : Ids of input tokens in the initial sentences
 v_{in} : Numeral values in the initial sentences
 m_{val} : Masks for values
 m_{pad} : Padding Masks

```
1: Initialize  $w \leftarrow w_{in}, v \leftarrow v_{in}$ 
2: while  $w[-1] \neq \text{<eos>}$  do
3:   # Prepare for next word/value prediction
4:    $n \leftarrow \text{prepare\_inputs\_for\_generation}(w, v, m_{val}, m_{pad})$ 
5:   # Embed the inputs
6:    $x_{input}[-m_v] \leftarrow \text{Embedding}(n_w)$ 
7:    $x_{input}[m_v] \leftarrow \text{Linear}(n_v)$ 
8:   # Pass through the AR Model
9:    $h_{rep} \leftarrow \text{Transformer\_Decoder}(x_{input}, m_{pad})$ 
10:   $w_{logits} \leftarrow \text{Linear}(h_{rep}[-m_{val}])$ 
11:  # Compute the word/value
12:   $scores \leftarrow \text{logits\_warper}(\text{logits\_processor}(w_{gt}, w_{logits}[:-1]), -1)$ 
13:   $y_w \leftarrow \text{multinomial}(\text{softmax}(scores))$ 
14:  # Use Diffloss Sampling Procedure in Alg5
15:   $y_t \leftarrow \text{diff.sample}(h_{rep}[:-1])$ 
16:  if  $n_{next}$  is a value then
17:     $v.append(y_t)$ 
18:  else
19:     $w.append(y_w)$ 
20:  end if
21: end while
22: return  $w, v$ 
```

Algorithm 5 Diffloss Sampling Procedure

Require:

h_{rep} : Hidden representations for conditional diffusion
 $T = 200$: Number of sampling steps

```
1: # Initialize noise, model kwargs and diffusion
2:  $y \leftarrow \text{randn}(h_{rep}.shape[0], \text{net.in\_channels})$ 
3:  $model\_kwargs \leftarrow \text{dict}(c = h_{rep})$ 
4:  $\text{diff} \leftarrow \text{GaussianDiffusion}(T)$ 
5:  $r \leftarrow \text{diff.p\_sample\_loop}(\text{net}, y, model\_kwargs)$  # Predicted denoised sample
6: return  $r$ 
```

C More Details about Dataset Processing

C.1 Dictionary for Diverse Domains and Tasks

In UniGenX, we utilize a straightforward vocabulary dictionary for representing SMILES strings and material formulas, without any specialized design. Each atom type from the periodic table and special characters in SMILES, such as ‘C’, ‘Cu’, ‘(’, ‘)’, ‘=’, are treated as individual tokens. This approach enables UniGenX to accurately parse atoms and infer two-dimensional SMILES information through character-wise attention on special characters. Consequently, UniGenX can be readily extended to other scientific domains by simply expanding the dictionary to include additional special characters, such as amino acid names for proteins and nucleic acid names for DNAs and RNAs.

The vocabulary dictionary also incorporates special tokens, which are crucial for UniGenX’s flexibility as a next-token prediction model across diverse domains. These tokens serve as domain indicators, such as <bof> for material formulas and <bos> for molecule SMILES. Extending UniGenX to other domains, like proteins and DNA, requires adding corresponding tokens, such as <boa> and <bod>. This design empowers UniGenX to handle various domains within a unified sequence representation. Thus, these domain-specific special tokens are integral to the vocabulary dictionary.

Furthermore, special tokens facilitate different tasks. For structure generation, <boc> denotes coordinates. For conditional generation of sequences and structures, property tokens like <bulk> for bulk modulus and <band> for band gap are used. These tokens, followed by property values, precede the molecule sequence and coordinates. This allows UniGenX to generate both sequences and structures conditioned on specific properties. Therefore, the special tokens in the vocabulary dictionary provide UniGenX with flexibility across domains and tasks.

C.2 Materials

The pretraining dataset comprises structures from the Materials Project [63], NOMAD [64], and OQMD [65, 66], widely used open-source databases for materials. We eliminated duplicates in the merged dataset, filtered out data with chemical formulas failing SMACT validation, and removed structures with formulas matching those in the MP-20, Carbon-24, and MPTS-52 test sets used for evaluation. The final pretraining dataset contained approximately 5.5M samples.

We evaluated UniGenX on three common material benchmark datasets: MP-20, Carbon-24, and MPTS-52. MP-20 consists of 45,231 stable inorganic materials from the Materials Project [63], representing most experimentally synthesized materials with up to 20 atoms per unit cell. Carbon-24 [67] includes 10,153 carbon materials, each with 6 to 24 atoms per unit cell. MPTS-52, an extension of MP-20, is a more challenging dataset comprising 40,476 structures with up to 52 atoms per unit cell, ordered by their earliest publication year. The dataset splits followed those described in [15] and [9].

To ensure data consistency, we sorted atoms and coordinates according to predefined rules. Coordinates were represented as fractional coordinates.

The parsed data format is as follows:

<bos> [n * sites] <coord> [3 * lattice] [n * frac_coords] <eos>

	MP-20	MPTS-52	Carbon-24
Train	27,136	32,380	6,091
Valid	9,047	–	2,032
Test	9,046	8,096	2,030

Table S1: Size of Material Dataset

C.3 Molecules Conformation Generation

For the small molecule conformation generation task, we utilized the GEOM single-molecule multi-conformation dataset. Following DMCG, we partitioned the dataset into training, validation, and test sets with an 8:1:1 ratio, distributing conformations for each molecule into their respective sets to ensure no overlap. This resulted in 1,374,737, 165,204, and 174,162 conformation data points for QM9 in the training, validation, and test sets, respectively. For the larger GEOM-Drugs dataset, we selected 2,000,024, 100,104, and 100,106 conformation data points for training, test, and validation.

During data processing, we converted molecules to Canonical SMILES and renumbered atoms to align their indices with the SMILES order. Special SMILES characters were directly tokenized. In UniGenX, we represent SMILES information as a sequence, rather than a graph, leveraging the transformer decoder’s attention mechanism to capture all inherent information. To address potential mismatches between atom order in SMILES and coordinates, we used Canonical SMILES to align these orders. All information is then represented as a linear sequence input to the model, enabling UniGenX to jointly train SMILES and coordinates, improving molecule understanding compared to sequence-to-structure-only training. The parsed data format is as follows:

```
<bos> [cano_smiles] <coord> [n * coords] <eos>
```

C.4 Unification task

We use the mixture of material pretraining dataset and QM9 mentioned above to pretrain UniGenX. By adjusting the ratio of the two datasets, the material dataset loops twice when the small molecule dataset loops once.

The parsed data format is as follows:

```
<bos> <mat> [n * sites] <coord> [3 * lattice] [n * frac_coords] <eos>
<bos> <mol> [cano_smiles] <coord> [n * coords] <eos>
```

C.5 Conditional Generation of Molecules

For the Conditional Molecule Generation task, we adhered to two settings, as described in [28] and [45]. Both settings utilize the QM9 dataset (approximately 137k samples), partitioning the training data into two halves: one for generator training and the other for classifier training. Consistent with [28], we employed a random seed of 42 for data splitting and utilized their classifier for testing, ensuring no overlap. Unlike [45], we did not perform property normalization. Instead, property values were treated as numeric values and transformed into three-dimensional vectors, which were directly appended to the input sequence. Notably, we trained a unified model, using the same

architecture for all properties, a departure from previous methods. Furthermore, unlike graph-based models, our approach does not require pre-sampling atom numbers, as the special token `<coord>` controls SMILES generation. Finally, our model employs a simple vocabulary dictionary, treating all SMILES characters, including special characters, as individual tokens (see Appendix C.1 for details).

The parsed data format is as follows:

```
<bos> <prop> [prop_val] [cano_smiles] <coord> [n * coords] <eos>
```

C.6 Conditional Generation of Materials

For conditional generation in the materials domain, we fine-tune a model that has been pretrained on large-scale materials data. The single-property datasets for bulk modulus and magnetization are taken directly from the [17]. For multi-property conditional generation, we curate a new dataset by filtering materials from the Materials Project and computing their properties using [19].

Each training sentence encodes a set of target properties through dedicated property tokens. Specifically, for a sample with k conditioning attributes, the input sequence includes k corresponding special tokens. The input sentence format is illustrated below:

```
<prop1> [prop1_val] <prop2> [prop2_val] <prop3> [prop3_val] <bos> [n * sites]
<coord> [3 * lattice] [n * frac_coords] <eos>
```

C.7 Protein and Emulating MD equilibrium distributions

To train our foundational protein model, we constructed a sequence of amino acid chains (represented by their single-letter abbreviations) for each protein. For the rare unconventional amino acids in the 'Emulating MD equilibrium distributions' section, we used the letter 'X' as a substitute. After generation, a proprietary post-processing procedure was applied to ensure their consistency and validity.

The full input sequence is organized as follows:

```
<bos> [n * Amino_acid] <coord> [n * C $\alpha$ _coords] <eos>
```

For the evaluation metrics, we first partitioned the 2D TICA projections into a grid of $num_bins \times num_bins$ along the x and y axes. We then counted the number of points falling into each bin, which can be interpreted as an unnormalized probability distribution $P(x, y)$. The free energy was subsequently computed using the Boltzmann relation:

$$F(x, y) = -k_B T \cdot \ln(P(x, y) + \epsilon). \quad (22)$$

To improve visualization, we offset the minimum free energy to zero and truncated extremely high energy values. This procedure yielded a more interpretable representation of the Free Energy Landscape.

C.8 Protein-Ligand Docking

For the protein-ligand docking task, we adopt a similar strategy to that used in the small molecule generation setting. Each small molecule is represented using its canonical SMILES string, while

protein pockets are described at the full-atom level, with atom order aligned to the residue indexing in the original MD.hdf5 files provided by [34]. The corresponding coordinate tensors are arranged to follow this atom sequence exactly.

To enable a single model to handle both the ligand-only and joint pocket-ligand generation tasks, we design a unified input sequence structure that encodes all relevant components. The full input sequence is organized as follows:

```
<bos> <bopo> [n * pocket_atoms] <eopo> <boapc> [n * apo_coords] <eoapc>
<bom> [cano_smiles] <eom> <bohpc> [n * holo_coords] <eohpc> <bomc> [n *
lig_docked_coords] <eomc> <eos>
```

During inference, task-specific tokens are used to control which parts of the structure the model is expected to generate. For the first task—ligand generation conditioned on both apo and holo pockets—the input sequence is provided up to the <bomc> token, allowing the model to autoregressively infer the subsequent ligand coordinates. For the second task—joint prediction of the holo pocket and ligand given only the apo pocket and SMILES—the input sequence is truncated at <bohpc>, prompting the model to predict both the holo pocket and downstream ligand coordinates.

Since the primary learning objective is to recover 3D coordinates, training is supervised using only the diffusion loss, applied to the predicted atomic positions. Following the design of 3D-MolFormer, we apply coordinate scaling as part of preprocessing. All 3D coordinates are scaled down by a factor of 5 to facilitate more stable and effective learning.

C.9 EC Number-guided Protein Generation

For training data, we used all protein sequences in UniProt that have an assigned EC number and corresponding structural information available in the AlphaFold Database (AFDB), and with sequence lengths below 512 residues. This results in a dataset of approximately 20 million samples.

The first three digits of the EC number are decomposed into three separate numbers. For example, "2.6.1.x" would be converted to 2 (ec number 1), 6 (ec number 2), and 1 (ec number 3).

```
<bos> <ec1> [ec number 1] <ec2> [ec number 2] <ec3> [ec number 3] [n *
amino_acids] <coord> [n * coords] <eos>
```

C.10 Instruction Tuning with Natural Language Model

To train our model to generate crystal structures from natural language instructions, we constructed a dataset using the following format:

```
<bos>Instruction: Generate a structure based on the provided composition ,
[n * sites].
Response: [3 * lattice] [n * frac_coords]<eos>
```

The <bos> and <eos> tokens delineated the start and end of the sequence, respectively, while the **Instruction:** and **Response:** labels clearly separated the input and output. By training on this structured data, the model learned to associate textual instructions with corresponding crystal structure representations, effectively bridging the gap between natural language and structural data.

D Computing Resource Usage

Table S2 details the GPU computational resource usage for various tasks, including task category, dataset, model size, GPU specifications, and total computational cost measured in GPU days. All experiments were conducted using either NVIDIA A100 (80G) or AMD MI300X (192G) GPUs. Unless otherwise specified, training was performed with BF16 precision for computational efficiency. The reported GPU days range from 0.9 (Carbon-24) to 191 (Unified Pretraining).

It is worth noting that during fine-tuning phases, smaller batch sizes were often used due to limited dataset sizes or task-specific constraints. As a result, GPU utilization was suboptimal, and the actual effective GPU compute required may be significantly lower than the reported GPU days if fewer GPUs were used in parallel.

Task	Data	Model	GPU	Cost (GPU Days)
Material	Pretrain	UniGenX(400M)	MI300X (192G)	109
	MP-20	UniGenX(400M)	A100 (80G)	2.2
	MPTS-52	UniGenX(400M)	A100 (80G)	2.6
	Carbon-24	UniGenX(400M)	A100 (80G)	0.9
Molecule	Large-QM9	UniGenX(400M)	A100 (80G)	26.6
	Large-Drugs	UniGenX(100M)	MI300X (192G)	128
Conditional Mol	QM9	UniGenX(100M)	A100 (80G)	12
Conditional Mat	Mag	UniGenX(400M)	A100 (80G)	<u>55.8</u>
	Bulk	UniGenX(400M)	A100 (80G)	<u>1.08</u>
	Multiple	UniGenX(400M)	MI300X (192G)	<u>4.72</u>
Unified	Pretrain	UniGenX(100M)	MI300X (192G)	191
Protein	Pretrain	UniGenX(400M)	MI300X (192G)	<u>853</u>
	MD	UniGenX(400M)	MI300X (192G)	<u>11</u>
	EC Number	UniGenX(400M)	MI300X (192G)	<u>41</u>
Docking	MISATO	UniGenX(100M)	MI300X (192G)	<u>67.7</u>

Table S2: GPU Training Cost per Task. Models trained with BF16 precision are underlined.

E Ablation Study

To elucidate the contribution of each component within our model, we performed a series of ablation studies. By systematically removing or altering key components, we aimed to evaluate their individual and combined impact on overall model performance. The core components examined were the data parser, backbone, and diffloss, responsible for data preparation, word and condition generation, and structure generation, respectively. In our ablation studies, we selectively removed or modified these components to analyze their contribution to the final performance.

E.1 Data Parser

In this section, we investigate the impact of modeling the space group (sg) on the performance of the model. Sg train refers to whether the space group information is modeled during the training process, with the aim of evaluating its contribution to the model’s prediction accuracy.

We kept the diff mul and res blocks parameters constant (at 16 and 12, respectively) and conducted a comparative experiment on whether to model the space group.

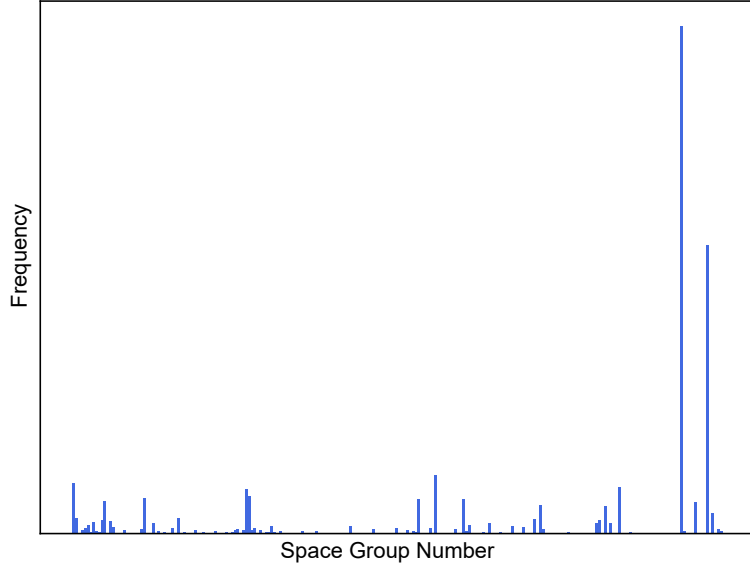


Figure S1: The distribution of the frequency of the space group in training data is imbalanced.

The experimental results shown in S3 indicate that the model performs slightly better without modeling the space group than when the space group is modeled, due to the imbalanced space group distribution as shown in S1. This may suggest that in this particular task, the space group information does not significantly help to improve the match precision and may even introduce some unnecessary complexity, limiting further enhancement of model performance.

Hence, we can conclude from this ablation study that although space group information might be beneficial for model performance in certain tasks, disabling sg allows the model to learn spatial

features more freely in the current task, thereby improving overall performance. In subsequent ablation studies, unless specifically mentioned, the space group will not be modeled.

Model	Diff mul	Res blocks	Sg	Match rate %
UniGenX(100M)	16	12	+	54.62
UniGenX(100M)	16	12	-	56

Table S3: Comparison of Model Performance with and without sg

E.2 Model Size

In this section, we conducted detailed experiments to investigate the impact of model size on the performance of the backbone. Specifically, we compared the performance of UniGenX(100M) and UniGenX(400M), and the experimental results are presented in S4. Meanwhile, different model size configurations are in S5

In the experiments, the main differences between UniGenX(100M) and UniGenX(400M) lie in the number of hidden layers and the number of attention heads. The experimental results show that as the model size increased from 100M to 400M parameters, there was an improvement in model performance. Specifically, the Match score for UniGenX(100M) was 57, while the Match score for UniGenX(400M) increased to 59.35. This indicates that increasing the number of hidden layers (from 6 to 24) enhanced the model’s feature representation capability and its ability to capture complex structures, under the same attention head configuration.

These experimental findings validate the advantages of larger models in complex tasks, particularly in terms of their ability to better extract and integrate information within multi-layered deep structures and rich contextual representations. However, it is important to note that while performance improvements are achieved, the increase in model size also brings higher computational costs. Therefore, in practical applications, balancing performance against computational expense is an important consideration.

The experiments consistently demonstrate that increasing model parameters, especially the number of hidden layers, has a positive impact on match precision.

Model	Diff mul	Res blocks	Match rate %
UniGenX(100M)	16	12	57
UniGenX(400M)	16	12	59.35

Table S4: Backbone parameters and performance.

Model	UniGenX(100M)	UniGenX(400M)
hidden size	1024	1024
intermediate size	4096	4096
num hidden layers	6	24
num attention heads	16	16
num key value heads	16	16

Table S5: Comparison of UniGenX(100M) and UniGenX(400M) model configurations

E.3 Diffloss

E.3.1 Diffmul & Resblocks

In the ablation study of the diff module, we experimented with two key parameters in the module, the diffmul and the resblocks, to assess their impact on model performance.

The diffmul, short for diffusion multiplier, represents the number of time points selected along the path where the model pushes the noise distribution forward to the data distribution. It controls the model’s ability to extract features along the diffusion path. We chose two different values, 4 and 16, to observe the impact of smaller and larger feature extraction capabilities on the final results. As shown in S6, it is obvious that the model performs better with a diffmul value of 16 compared to a value of 4. For example, with res blocks fixed at 3, increasing the diffmul from 4 to 16 improved the Match score from 53.31 to 56.06. Similarly, with res blocks at 12, the Match score for a diffmul of 16 (54.62) was higher than that for a diffmul of 4 (48.98). This suggests that a greater feature extraction capability performs better in handling complex structures.

Resblocks refer to the number of residual blocks, which are used to enhance the model’s expressive power. We compared the performance between models with 3 and 12 Resblocks, observing mixed effects on performance. With space group modeling, a model size of 100M, and a Diffmul of 4, increasing the number of Resblocks from 3 to 12 led to a decrease in Match Rate from 53.31% to 48.98%. However, with a Diffmul of 16, the performance difference between 3 and 12 Resblocks was marginal (56.06% vs. 54.62%). On the other hand, when increasing the model size from 100M to 400M and not modeling the space group, increasing Resblocks from 3 to 12 improved performance from 54.78% to 59.35%. These results suggest that while increasing the number of Resblocks helps the model handle more complex input data, the performance gains may plateau in certain conditions.

In summary, the experimental results demonstrate that increasing the values of diffmul and resblocks significantly contributes to enhancing the overall performance of the model.

Model	Diffmul	Resblocks	Sg	Match rate %
UniGenX(100M)	4	3	+	53.31
UniGenX(100M)	16	3	+	56.06
UniGenX(100M)	4	12	+	48.98
UniGenX(100M)	16	12	+	54.62
UniGenX(400M)	16	3	-	54.78
UniGenX(400M)	16	12	-	59.35

Table S6: Experimental Results of Diffloss Module Configurations

E.3.2 Scheduler

In this section, we explore the impact of two schedulers on the effectiveness of the model. The two schedulers are the Diffusion scheduler used in this paper and the EDM scheduler, which was first introduced in [54].

The EDM scheduler utilizes a second-order Heun ODE solver for improved sampling accuracy and efficiency. The time step scaling follows a specific schedule based on $(\sigma_{max}^{\frac{1}{\rho}} + \frac{1}{N-i}(\sigma_{min}^{\frac{1}{\rho}} - \sigma_{max}^{\frac{1}{\rho}}))^{\frac{1}{\rho}}$, allowing for smooth transitions during the diffusion process. EDM employs a flexible network architecture, enabling compatibility with various models. Key preconditioning techniques include skip scaling, defined as $\sigma \cdot \sigma_{data}/(\sigma_{data}^2 + \sigma^2)$, along with tailored input and output scaling

formulas that optimize noise and signal propagation. The noise distribution is modeled as $\ln(\sigma) \sim \mathcal{N}(P_{\text{mean}}, P_{\text{std}}^2)$. Loss weighting is also balanced with the formula $(\sigma_{\text{data}}^2/(\sigma_{\text{data}}^2 + \sigma^2))^2$. More details can be found in [54].

EDM parameters We provide three images showing the Match rate under different **std**, **sig**, and **mean** values in S2. The default model setting is UniGenX(100M) with 12 resblocks and 16 diffmul. Here is a summary of the main trends:

Impact of the mean value:

- The match rate tends to be higher, typically maintaining above 0.58 to 0.6, when the mean value fluctuates between -1.4 and -0.8. A relatively lower mean value seems to correlate with a higher match rate.
- When the mean value decreases to -1.6, the match rate sometimes drops slightly but the overall performance remains relatively stable.
- Larger mean values (e.g., -0.8) usually perform better in terms of match rate, and as the mean value becomes smaller (e.g., -1.6 or lower), the match rate may gradually decrease.

Impact of std (standard deviation):

- The match rate usually remains stable when std fluctuates between 1 and 1.7. The smaller the std value (e.g., 1), the match rate tends to be slightly higher.
- When the std variation is small (e.g., from 1 to 1.5), fluctuations in the match rate are not significant, suggesting that std has a minimal impact on the match rate within this range.
- As std further increases to 1.7, the match rate begins to decline slightly, but not significantly.

Impact of sigma value:

- The closer the sig value is to 1, the better the match rate typically performs, often fluctuating between 0.58 and 0.6 when the value is 1.
- When the sig value is 1.3, the match rate sometimes decreases slightly but still maintains a relatively high level.
- Lower sig values (e.g., 0.2 or 0.5) are usually accompanied by lower match rates, indicating that lower sig values may inhibit the model's matching ability.

Multifactorial influence:

- For the combination of mean = -1.4, std = 1.2, and sig = 1, the match rate can reach a peak of 0.6024.
- As std and sig increase to higher values, the match rate typically declines, e.g., when sig increases to 1.5, there is a slight decrease in the match rate.
- A combination of particularly low sig and larger mean (e.g., mean = -1.6, sig = 0.2) results in a sharp decline in the match rate.

In summary, the data suggest that moderate mean and std values combined with a higher sig value can enhance the match rate, while more extreme combinations of mean and sig tend to lower the match rate.

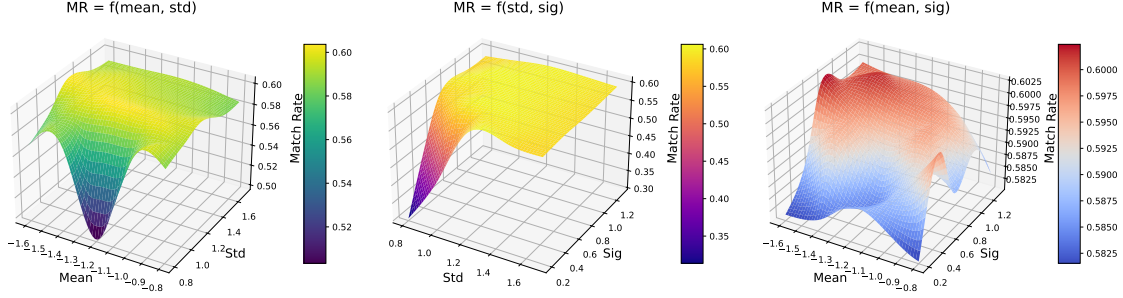


Figure S2: Comparison between mean, std and sigma in EDM

DDPM vs. EDM We compare Diffloss and EDMloss in S7, and the analysis of the table is as follows.

Despite the fact that the EDM scheduler slightly outperforms the Diffusion loss in its best results, the values of key parameters such as **sig**, **mean**, and **aug** for conditional diffusion are challenging to determine accurately. This introduces a large number of parameter combinations in EDM, requiring extensive hyperparameter tuning. Moreover, after incorporating data augmentation, we observed that the performance gap between EDM and DDPM training strategy becomes minimal. In this work, we mainly focus on the combination of the auto-regressive model and the diffusion head in a unified generation across different tasks and different domains. Hence, here we adopt the DDPM training strategy for its simplicity, requiring fewer hyperparameters to be tuned. To achieve better performance, an investigation of combining different setups of other diffusion strategies or flow matching models is also supported but not included in this work.

Model	Diffmul	Resblocks	Scheduler	Augmentation	MR %
UniGenX(400M)	16	12	DDPM	-	59.35
UniGenX(400M)	16	12	EDM	-	59.08
UniGenX(400M)	16	12	DDPM	+	63.88
UniGenX(400M)	16	12	EDM	+	63.00

Table S7: Ablation study on Scheduler and Augmentation.

E.4 Data Augmentation

In this section, we investigate the impact of data augmentation on model performance. The augmentation techniques employed include unit cell translation and rotation. For unit cell translation, a random three-dimensional vector is added to the fractional coordinates of each atom, and the result is taken modulo 1 to maintain periodicity. Conversely, unit cell rotation involves randomly rotating the lattice coordinate system while keeping the atomic coordinates fixed. Algorithm 6 presents the pseudocode for material data augmentation.

As shown in Table S7, incorporating augmentation significantly enhances performance for both schedulers, resulting in an approximate 4-point increase in match score.

Algorithm 6 Rotation & Translation Augmentation

Require:

l : Lattice
 x : Fractional Coordinates
1: **# Apply Rotation**
2: $R \leftarrow \text{UniformRandomRotation}()$
3: $l \leftarrow R \cdot l$
4: **# Apply Translation**
5: $t \sim \mathcal{N}(\vec{0}, \mathbf{I}_3)$
6: $x \leftarrow (x + t) \bmod 1$
7: **return** l, x

E.5 Pretraining or Training from Scratch

In this section, we present an ablation study comparing the impact of pretraining versus training from scratch across three datasets: MP-20, Carbon-24, and MPTS-52. Table S8 summarizes the results, detailing Match Rate (MR) and Root Mean Square Deviation (RMSD).

The pretrained base model exhibits moderate performance across the datasets, achieving a Match Rate (MR) of 60.48% on MP-20, 3.15% on Carbon-24, and 33.61% on MPTS-52, with corresponding RMSD values of 0.0568, 0.1928, and 0.1086, respectively.

Training the model from scratch yields a slight improvement in MR for MP-20, reaching 63.88%, but demonstrates mixed results on Carbon-24 and MPTS-52, with MR decreasing to 27.09% and 29.09%, respectively.

Conversely, finetuning the pretrained model on each dataset results in superior performance, with substantial enhancements in MR across all three datasets. On MP-20, the finetuned model achieves an MR of 67.01%. Similarly, on Carbon-24 and MPTS-52, the finetuned model achieves MR values of 30.05% and 38.65%.

These findings suggest that pretraining followed by dataset-specific finetuning is a more effective strategy than training from scratch, particularly for complex datasets like MP-20 and MPTS-52. Notably, even when trained from scratch, UniGenX outperforms FlowMM on these three benchmarks, demonstrating the inherent advantages of UniGenX.

	MP-20		Carbon-24		MPTS-52	
Methods	MR(%) \uparrow	RMSD \downarrow	MR(%) \uparrow	RMSD \downarrow	MR(%) \uparrow	RMSD \downarrow
Base Model	60.48	0.0568	3.15	0.1928	33.61	0.1086
Train from Scratch	63.88	0.0598	27.09	0.2264	29.09	0.1256
Finetune on Each	67.01	0.037	30.05	0.2286	38.65	0.0657

Table S8: Pretraining or Training from Scratch.

F Special Tokens Used in Sequence Modeling

In our model framework, we introduce a set of special tokens to indicate the beginning of different modalities. These tokens serve as explicit prompts for the model to distinguish between different input types, such as molecular SMILES, protein sequences, and geometric structures. Table S9 provides a summary of the special tokens used in our vocabulary.

Token	Description
<bos>	Beginning of sites/sentence/SMILES
<eom>	End of sentence
<bof>	Beginning of material formula
<bol>	Beginning of material lattice
<bop>	Beginning of protein amino-acid sequence
<boc>	Beginning of coordinates
<bulk>	Beginning of the property bulk modulus
<band>	Beginning of the property band gap
<mag>	Beginning of the property magnetic
<heat_capacity>	Beginning of the property heat capacity
<E_hill>	Beginning of the property energy above the convex hull
<density>	Beginning of the property density
<bopo>	Beginning of pocket
<eopo>	End of pocket
<boapc>	Beginning of pocket apo coords
<eoapc>	End of pocket apo coords
<bom>	Beginning of molecule SMILES sequence
<eom>	End of molecule SMILES sequence
<bohpc>	Beginning of pocket holo coords
<eohpc>	End of pocket holo coords
<bomc>	Beginning of molecule coords
<eomc>	End of the molecule coords
<ec1>	Beginning of the EC Number 1
<ec2>	Beginning of the EC Number 2
<ec3>	Beginning of the EC Number 3

Table S9: Explanation of special tokens used in the unified vocabulary.